UNIVERSITY OF CALIFORNIA, SAN DIEGO

3D Printing Functional Nanocomposites

A thesis submitted in partial satisfaction of the requirements for the degree Masters of Science

in

Nanoengineering

by

Yew J. Leong

Committee in charge:

Professor Shaochen Chen, Chair
Professor Yi Chen
Professor Donald Sirbuly

2016

The thesis of Yew J. Leong is approved, and it is acceptable in quality and form for publication on microfilm and electronically:

_____

_____

_____

Chair

University of California, San Diego

2016

Table of Contents

List of Figures

Acknowledgements

I would like to thank Dr. Shaochen Chen for being my being my advisor and giving me the opportunities to do the work presented in this thesis. I would also like to thank all the members in my lab for helping me throughout my time in lab during both undergraduate and graduate years. I would also like to thank Dr. Yi Chen and Dr. Donald Sirbuly for being in my committee as well.

Chapter 2, in part is currently being prepared for submission for publication. Leong, Y., Chen, S. This thesis author was the primary investigator and author of this material.

Section 3.1, in part, is a reprint of the material as it appears in Zhu, W., Li, J., Leong, Y., Rozen, I., Qu, X., Dong, R., Wu, Z., Gao, W., Chung, P., Wang, J. & Chen, S. 3D-Printed Artificial Microfish. *Adv. Mater.* **27**, 4411-4417 (2015). The thesis author was the third author of this paper.

Section 3.2, in part, is currently being prepared for submission for publication of the material. Leong, Y., Chen, S. This thesis author was the primary investigator and author of this material.

ABSTRACT OF THE THESIS

3D Printing Functional Nanocomposites

by

Yew J. Leong

Masters of Science in Nanoengineering

University of California, San Diego, 2016

Professor Shaochen Chen, Chair

3D printing presents the ability of rapid prototyping and rapid manufacturing. Techniques such as stereolithography (SLA) and fused deposition molding (FDM) have been developed and utilized since the inception of 3D printing. In such techniques, polymers represent the most commonly used material for 3D printing due to material properties such as thermo plasticity as well as its ability to be polymerized from monomers. Polymer nanocomposites are polymers with nanomaterials

composited into the polymer matrix. Nanocomposites possess superior properties compared to its pure polymer form due to the nanomaterials imparting its unique qualities onto the nanocomposite. Combining the capabilities of 3D printing and the properties of nanocomposites could potentially unlock countless possible applications.

In this thesis, we present the ability to 3D print functional nanocomposites using two printing systems: “micro continuous optical printing” (μCOP), an in-house developed system that utilizies a digital micromirror device (DMD) in a SLA based process for rapid optical 3D printing, and two photon polymerization (TPP) which involves a femtosecond laser to fabricate 3D structures with ultrahigh precision and micron-nano scale resolutions. Chapter 2 of this thesis showcases the 3D printing ability of the μCOP system. Microcones and size tunable microwells were printed in a parallel manner with high speeds and resolutions. Chapter 3.1 of this thesis uses the μCOP system to 3D print artificial microfishes with encapsulated platinum (Pt) nanoparticles and magnetic (Fe_3O_4) nanoparticles for locomotive and magnetically guided purposes. The speeds of the microfishes can be tuned through the geometrical design of the microfish as well as through the concentration of the encapsulated Pt particles. Additional detoxifying nanoparticles (PDA) were encapsulated in the microfishes and displayed detoxification abilities. Chapter 3.2 of this thesis is a work in progress that uses the TPP system to 3D print highly defined piezoelectric nanocomposites using 20nm $BaTiO_3$ (BTO) nanoparticles and a bisphenol-A (BPA) free photopolymerizable polycarbonate (PC). The printed structures display high uniformity across all printed areas with resolutions down to 1-2μm. The BTO

nanoparticles in the nanocomposites do not interfere with the printing capabilities of the TPP system allowing the system to retain its high precision capabilities

Chapter 1: Introduction

3D printing brought the prospect of rapid prototyping and rapid manufacturing where designs could be easily made through the use of 3D computer models. It has found applications in areas such as the aerospace industry[1] and the biomedical industry[2]. Many processes have been developed over the years and some have displayed the ability to print microstructures. Stereolithography (SLA) has shown the capability of fabricating components for microelectromechanical systems[3]. Fused deposition modeling (FDM) has been used to print Li-ion microbattery architectures with incredibly high areal energy and power densities. Selective laser sintering (SLS) has been used to fabricate a transparent flexible metal grid conductor[4]. In this thesis we present the use of two 3D printing systems to 3D print functional nanocomposites. Nanocomposites can be defined as a bulk solid material that comprises of multiple phases with at least one of the phases consisting of one dimension <100nm[5]. This imparts unique changes in bulk material properties such as changes in mechanical or electrical properties[6–8]. The first 3D printing system that will be described is an in-house developed system called "micro continuous optical printing" (μCOP), which involves the use of a digital micromirror device (DMD) in a SLA based process for rapid optical 3D printing. The second system is a two photon polymerization (TPP) system which involves a femtosecond laser to fabricate 3D structures with ultrahigh precision and micron-nano scale resolutions[9]. The rest of this chapter will introduce the concepts and principles of μCOP and TPP as well as the concept of nanocomposites.

1.1 Micro continuous optical printing (μCOP)

μCOP is a SLA based system for rapid optical 3D printing that we have developed in the past to allow us to print a variety of complex micro 3D geometries and structures with high speeds and high resolutions[10–13]. The μCOP system is illustrated in **Figure 1.1 a**. The key component of our system is the DMD, which consists of an array of about 2 million micro mirrors which can all be individually controlled to project a desired 2D image, which is illuminated by UV light, onto a solution of photopolymerizable resin to print highly specified 3D structures with detailed designs and features. The μCOP system utilizes an in house developed computer-aided 3D printing system which flexibly allows us to project digital images on the fly onto the photopolymerizable resin. The resin is loaded onto a motorized *x*-*y*-*z* stage (Newport 426/433 series) that is coupled to the computer-aided system as well. This allows us to rapidly print complex 3D structures with ease. An example image for a simple gridded structure is shown in **Figure 1.1 b.** Such an image can be easily made from any image creating or editing software such as Adobe Photoshop. The white portions of the image are projected onto the resin, which photopolymerizes into 3D structures. Conversely, the black portions of the image are not projected onto the resin, which leaves those portions unpolymerized. All works in this thesis used a glass substrate functionalized with 3-(trimethoxysilyl)propyl methacrylate (Sigma-Aldrich), as described in another work,[14] to assist attachment of the printed structures onto the substrate. The focal plane of the image is projected directly on the bottom side of the substrate. All works in this thesis used PDMS spacers with specific heights that were

placed in between the glass substrate and the stage to determine the maximum height of the printed structures.

1.2 Two-photon polymerization (TPP)

Two-photon polymerization (TPP) is a unique 3D printing technique that is capable of fabricating on micron-nano scale with ultrahigh precision[9] with reported resolutions in the sub-100nm region[15] . TPP has found use in fabricating 3D photonic crystal structures[16] fabricating 3D hydrogel scaffolds to study cell migration[17]. The TPP system is illustrated in **Figure 1.2.** Photopolymerization in this system is only induced when the photoinitiator simultaneously absorbs two photons. Only a small portion in the center of the focused laser spot with high intensity and energy is able to induce the absorption of two photons. Using a photoinitator that is capable of two-photon absorption with a peak absorption of 400nm, TPP essentially allows the use of an 800nm laser to induce photopolymerization, as the energy of two 800 nm photon is equivalent to one 400nm photon. These unique properties give two photon polymerization high penetration and selectivity of printing within the photopolymerizable resin. By coupling the laser in conjunction with a computer aided 3D design, the focused laser beam for TPP can be used to fabricate a wide variety of 3D structures with great precision and resolutions. In the work presented within this thesis, the laser in use for TPP is a Ti:sapphire femtosecond laser with 800 nm wavelength, 10-fs pulse width, with a repetition rate of 80 Mhz. Laser power and writing speeds were adjusted accordingly with a laser beam attenuator and by specifying stage movement speed.

a)

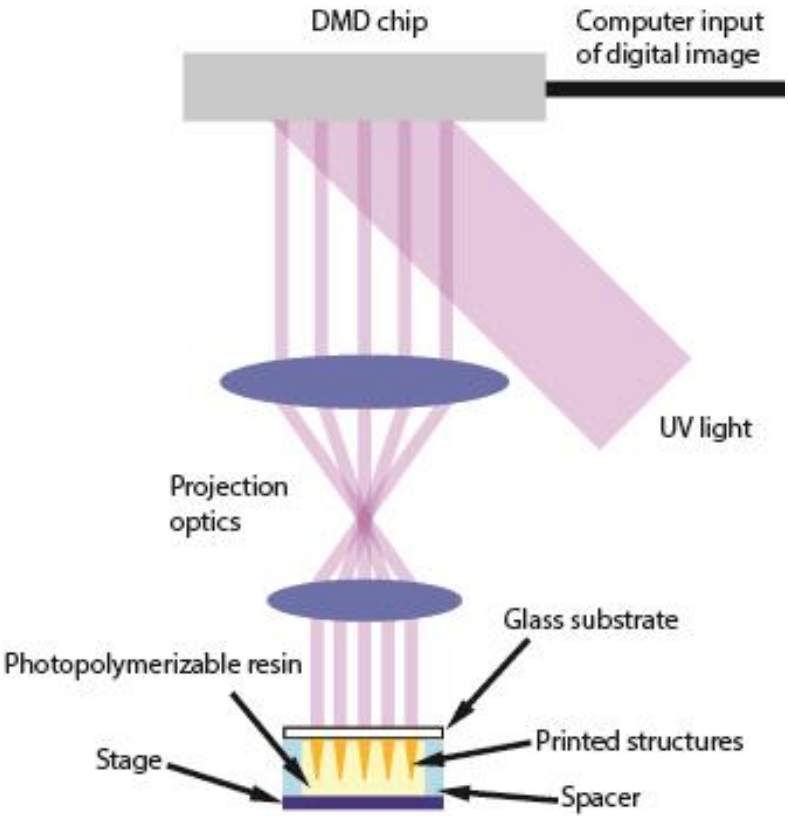

b)

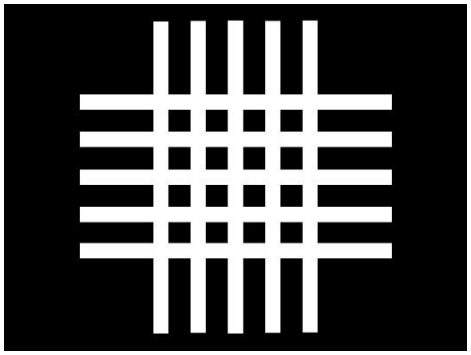

Figure 1.1: a) Schematic of the µCOP system that consists of a DMD with digital image input coming from a computer, UV light source, projection optics to focus the light onto the photopolymerizable resin, a motorized *x*-*y*-*z* stage, and spacers to determine the maximum height of printed structures. b) Example image used to 3D print with µCOP, where white portions are projected onto the resin while the black portions are not

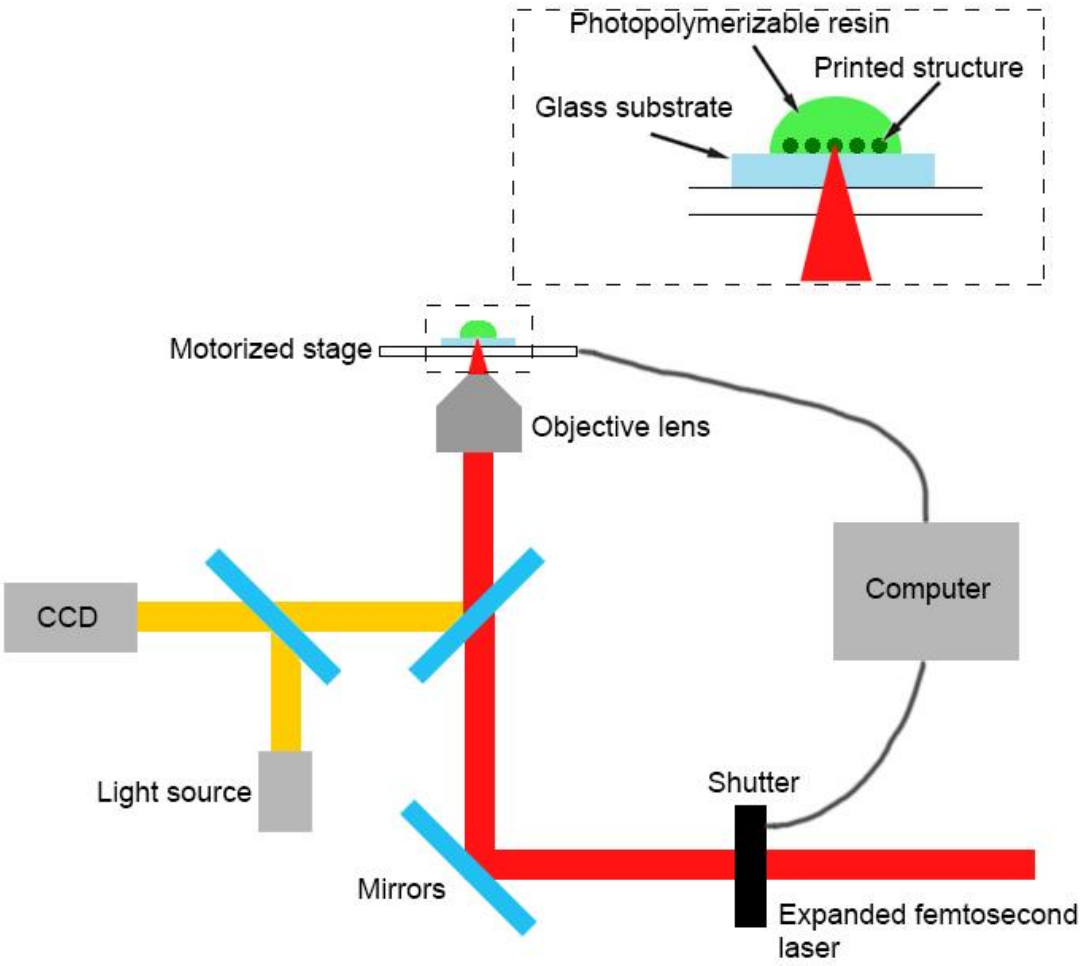

Figure 1.2: Schematic of TPP system. Only a small portion in the center of the focused laser spot with high intensity and energy is able to induce the absorption of two photons, allowing the fabrication of a wide variety of 3D structures with great precision and resolutions.

1.3 Nanocomposites

Nanocomposites can be defined as a bulk solid material that comprises of multiple phases with at least one of the phases consisting of one dimension <100nm[5]. Nanocomposites, especially polymer nanocomposites, provide superior properties when compared to its pure polymer form due to the nanomaterials imparting unique properties to the bulk material[18], prompting heavy research into nanocomposites. Nanocomposites can alter the mechanical properties dramatically. For example, nano layered clay in poly(vinyl alcohol) have been shown to drastically increase its stiffness and tensile strength[8]. Electrical properties such as ion diffusivity in the polymer electrolyte of Li-ion batteries have been improved with the use of nanocomposites[6]. Functionality can be added into the polymer as shown in the work where a flexible nanocomposite piezoelectric strain sensor comprised of ZnO nanorods grown on cellulose fibers showed good strain sensitivity[19]. Despite showing incredible potential, research into 3D printing nanocomposites have been sparse[20–22].Combining the superior material qualities derived from nanocomposites and the ability to easily design and manufacture 3D designs with 3D printing, could potentially unlock countless possible application[23]. In this thesis, we demonstrate the ability to 3D print functional nanocomposites with the use of μCOP and TPP. The nanoparticles used in this thesis were encapsulated in the polymer matrix by mixing it with the photopolymerizable polymer followed by polymerization with the μCOP or the TPP system. These systems allow for high spatial selectivity of where to encapsulate nanoparticles, allowing for highly defined 3D printable nanocomposites.

1.4 Overview

Using the μCOP and TPP systems as described in the previous sections, works showing the ability to 3D print nanocomposites will be presented in this thesis. Chapter 2 of the thesis showcases the ability of μCOP to 3D print structures without any nanoparticles. High printing speeds and resolutions were achieved with the μCOP along with a great amount of flexibility to print a wide variety of geometries. Chapter 3.1 of the thesis uses the μCOP system to 3D print artificial nanocomposite microfishes with encapsulated platinum (Pt) nanoparticles and magnetic (Fe_3O_4) nanoparticles for propulsion and magnetic guidance. The μCOP system was able to spatially determine where to encapsulate the nanoparticles, allowing for the integration of multifunctional capabilities in the microfishes. Chapter 3.2 of the thesis uses the TPP system to 3D print a piezoelectric polycarbonate nanocomposite. The nanocomposite comprises of 20nm $BaTiO_3$ (BTO) nanoparticles loaded into a photopolymerizable polycarbonate (PC). The TPP system provides high precision and resolutions for 3D printing in both pure PC and BTO-PC nanocomposite.

Chapter 2: Rapid 3D Printing of Tunable Microcone Array with Smooth Sidewall

Standard 3D printing techniques, stated in the previous section, such as SLA, FDM, SLS have shown broad application and has shown to be useful in different areas of interest. However, these techniques are serial by nature and can be relatively slow. In this work we report the use of our μCOP system to optically 3D print microcone arrays with size tunable microwell on the tip in a parallel manner to show case the ability of our system to rapidly print structures with high speeds and resolutions as well as the flexibility to print a different types of structures with great control.

Microcones have been made in other works in the past using a traditional SLA method utilizing a laser[3,24], but being able to print these structures in parallel with increased speeds are more desirable than printing them in a slower serial manner. Microwells are microstructures that could be used for single cell studies with well diameters ranging from 10μm up to >100μm[25]. These structures are typically made through the use a master stamp and a polydimethylysiloxane (PDMS) mold by utilizing photolithography and soft lithography methods[26,27]. Being able to directly print microwells cuts out the need of a clean room and reduces the cost and time spent needed to make the microwells, giving our process an edge over the current methods.

The UV light source (Omnicure 2000) used in this work projects a wavelength of 365nm and a total output intensity of 6.63 W cm^{-2}. The photopolymerizable resin used in this work is dipentaerythritol pentaacrylate (DPPA, Sartomer Inc.) with 1% (wt/vol) Irgacure 819 (Ciba Inc.). We choose DPPA because it's a fast curing polymer

due to its five acrylate groups in each monomer. It is also highly cross-linked after polymerization, making stiff and easy to handle after printing. DPPA has also been used as a mold for poly-ethylene glycol diacrylate structures[28], giving us flexibility with the directions of future investigations. 3-(trimethoxysilyl)propyl methacrylate (Sigma-Aldrich) was used to functionalize the glass substrate as previously described in another work[14]. The focal plane of the image is projected directly on the bottom side of the substrate. PDMS spacers 300µm in height were placed in between the glass substrate and the stage to determine the maximum height of the printed structures.

A hexagonal array of microcones as well as a spacing gradient array of microcones were printed. The images used for these arrays are show in **Figures 2.1 a** and **b** respectively. A scanning electron microscopy (SEM) image of the respective arrays are shown in **Figures 2.1 c, d.** For both arrays, the exposure times were 3.8s to fabricate the entire microcone arrays each. After exposure, the substrates were removed from the stage and the printed structures were washed with isopropyl alcohol to remove all the unpolymerized resin. The measured base diameter of each microcone is 100µm with a measured height of 288µm. In the hexagonal array, the spacing between each microcone is 300µm. In the spacing gradient array, the spacing between each microcone on width axis of the array is 258µm while the spacing between each microcone on the length axis of the array starts at 126µm and subsequently increases 30µm after each microcone. A close up of a microcone is shown in **Figure 2.2 a,b**. It is reasonable to think that the printed structures should be cylindrical in shape due to the fact that the 2D image being projected through the resin is circular, but this is not the case. This is due to two reasons. Firstly, the light intensity of any illuminated spot

a)

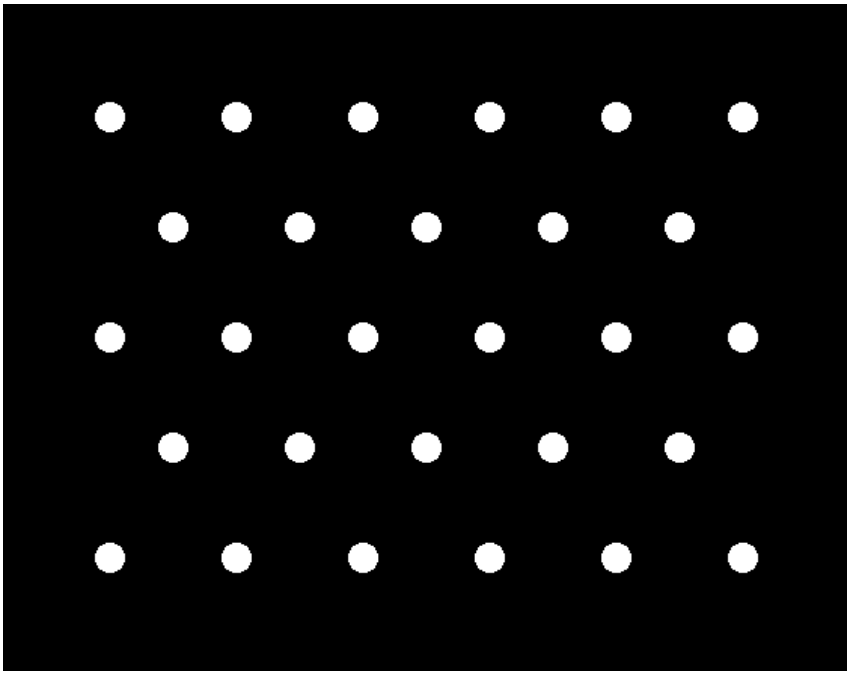

b)

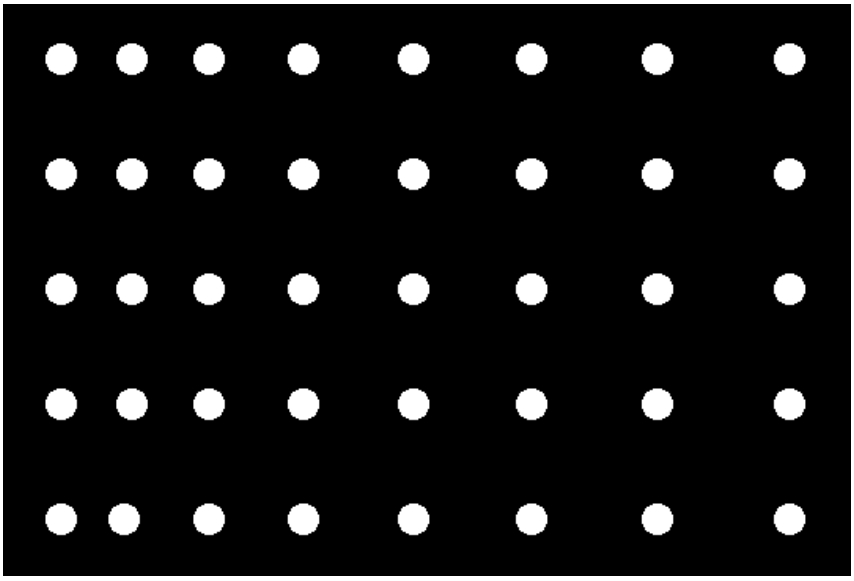

Figure 2.1: a) Image used to 3D print hexagonal array, b) Image used to 3D print gradient spacing array

c)

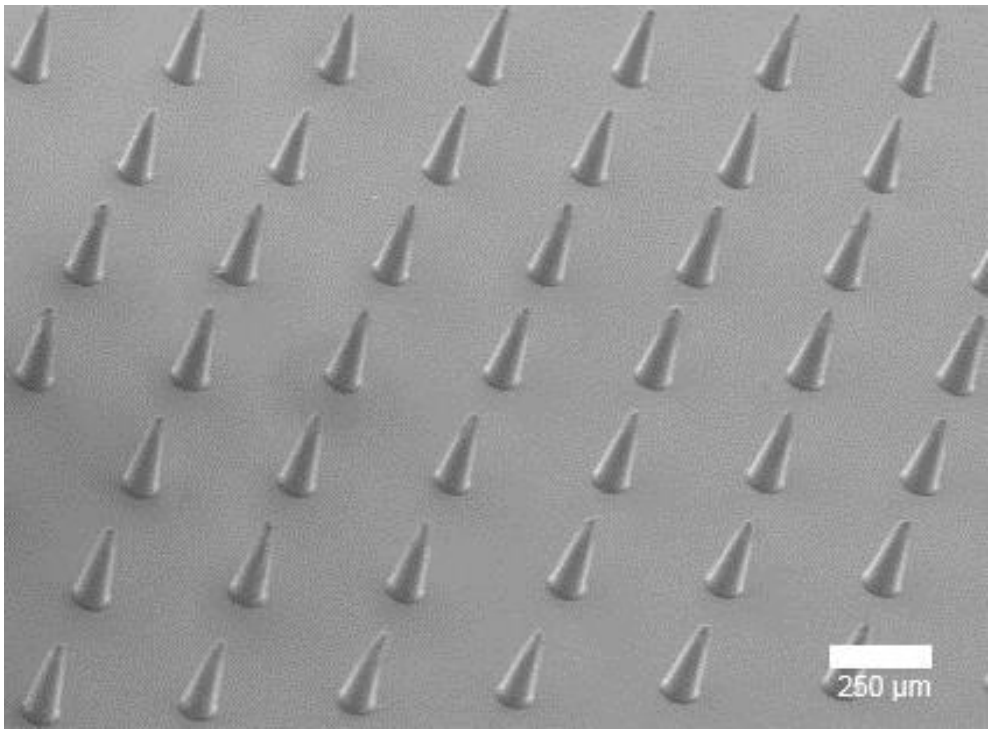

d)

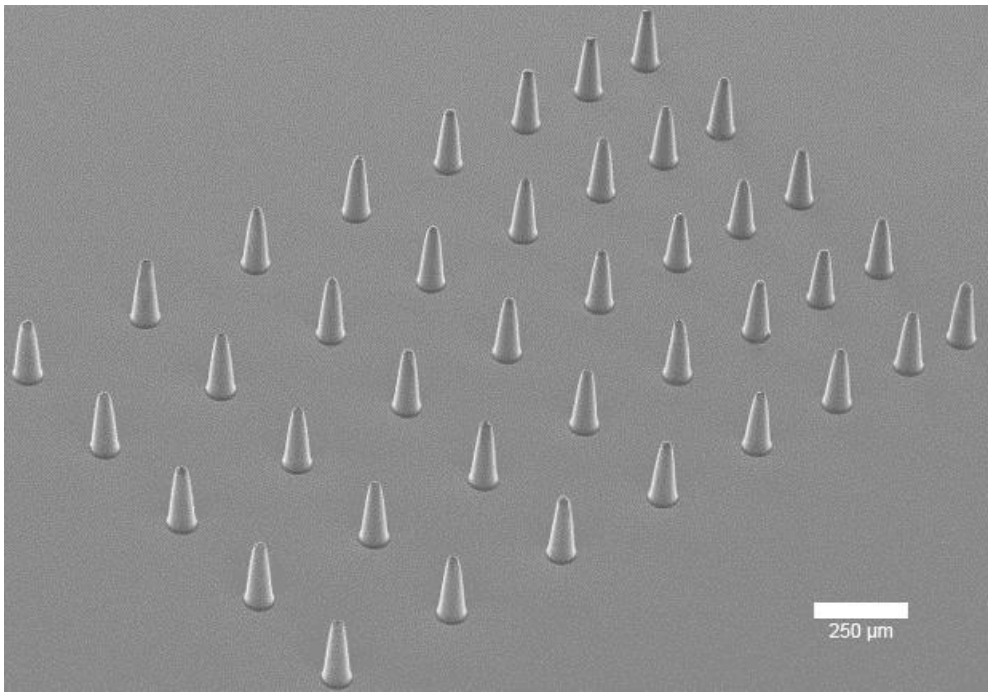

Figure 2.1: c) SEM image of the printed hexagonal microcone array, d) SEM image of the printed spacing gradient array, Continued.

can be described as a *point-spread function* and can be approximated as a Gaussian distribution[29]. This gives the center of any light spot the greatest relative intensity. Secondly, the resin follows Beer's law as the resin absorbs UV light resulting in the intensity dropping off greatly as the light continues to penetrate the resin. This results in the microcones being printed instead of microcylinders. The printed microcones also present smooth side walls, unlike the visible defined layers that characteristic in other common 3D printing techniques such as FDM and traditional SLA. Our μCOP system is responsible for this property as it prints in a layerless fashion by keeping the stage height constant throughout the printing process, instead of printing multiple layers by moving the stage height in discrete steps like how it is done in FDM and SLA. The smooth side walls give our system a greater edge over other systems and techniques as it improves the mechanical integrity of the 3D part by eliminating the artificial interfaces between the drops or layers in a nozzle-based 3D printing process,. The high uniformity of the array, speed of printing, high resolution, as well as ability to print smooth side walls shows the capability of the μCOP system.

Because the UV light absorption in the resin follows Beer's Law, the exposure time controls the amount of polymerization that occurs, and in turn controls how the structure is ultimately shaped. By further increasing the exposure from 3.8s through to 4.2s, the tip of the microcones showed interesting features. With an exposure of 4.0s, a dimple seemingly formed on the tip of the microcone as shown in **Figure 2.2 c**. Increasing the exposure up to 4.2s resulted in the formation of an opening on the tip of the microcone, a microwell, as shown in **Figure 2.2 d**. The microwell openings were

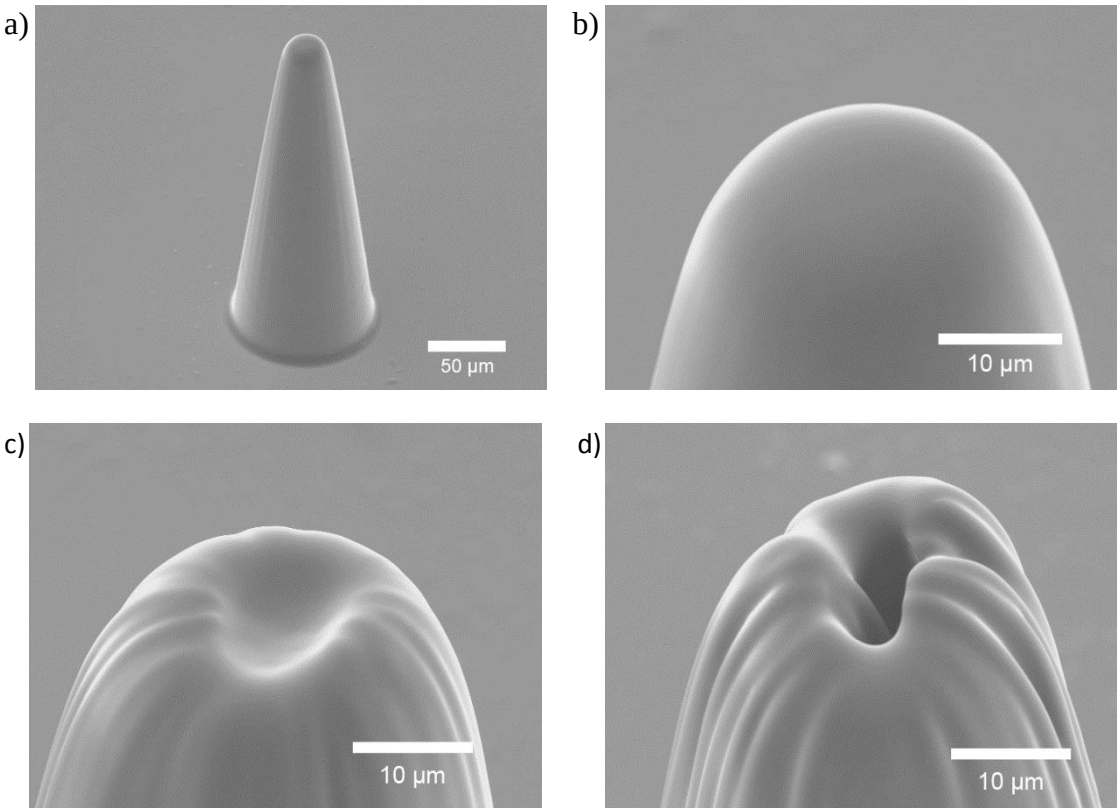

Figure 2.2: Close up of the printed microcones and the tips/microwell with different exposure times. a and b) 3.8s. c)4.0s. d)4.2s

measured to be 5µm in diameter. From the transition of exposures times from 3.8s through to 4.2s, a more favorable polymerization around the tip of the cone instead of the center of the tip is seen, resulting in the formation of the microwell. Also, compared to the smooth tip of **Figure 2.2 b**, the tips in **Figures 2.2 c,d** have rough aberrations around the tips. This might be caused by unintended photopolymerization from UV light being reflected from the already polymerized structures onto the periphery of the tip. This could also explain the formation of the microwells on the tip as the reflected light might have caused further polymerization on the periphery. This showcases the flexibility of the µCOP system as the features of the printed structures were altered by changing the exposure time of the structures.

In order to further examine the ability to control the fabrication and tune the size of these microcones and microwells using the µCOP system, an image with intentionally designed holes, as shown in **Figure 2.3 a,** was loaded onto the DMD and printed. Up close SEM images of one of the printed structures in the array is shown in **Figures 2.3 b**. The exposure time was 3.8s and the structures were washed in the same manner as previously described. The measured base diameter of the microcone is 88µm and the measured height is 105µm. The microwell opening on the tip of the cone is measured to be 11µm in diameter. The height of the microcones is shorter, compared to the measured height of previously printed microcones even though the exposure time was the same. This is due to less UV light entering the system, resulting in less photopolymerization and a shorter microcone. Similar to the previously printed microcones, these microcones also exhibit smooth side walls as these microcones are printed in a layerless fashion too. With the image being used, it is reasonable to predict

a)

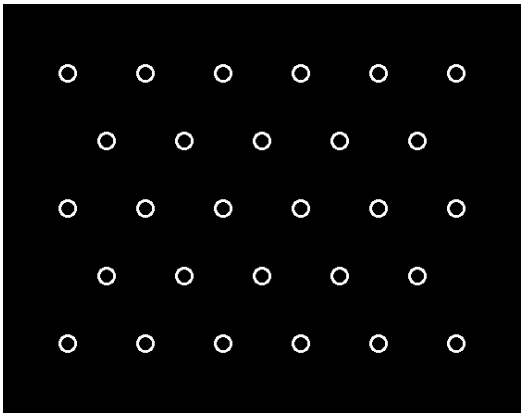

b)

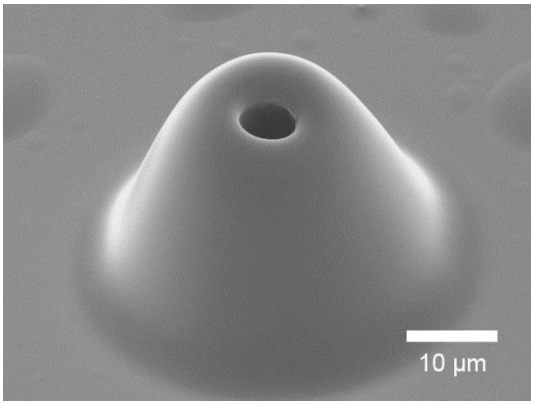

Figure 2.3: a) Image with holes designed. b) Close up view of the microcone

that the printed structures would have a larger hole diameter relative to the base diameter of the microcone compared to what was currently printed, but this is not the case due to the Gaussian distribution of the light intensity, as explained and described before. The intensity of light gradually goes to zero past the intended line width of the projected image, photopolymerizing portions past the intended image. This underlying principle explains why the size of the hole is smaller than expected. Just by simply changing the design in the image used for the printing, our μCOP system was able to control the dimensions and the design details of the printed microcones and microwells on the tip, allowing us to tune the structures to the specific needs at hand.

In conclusion, the μCOP system is fully capable of 3D printing microcones with high speeds and resolutions along with a high degree of control and flexibility. The microcones exhibit smooth side walls as they are printed in a layerless fashion. The tips on the microcones can be closed or opened to produce microwells and their sizes are tunable by changing the exposure times as well as changing the design of the image being projected. Many other geometries and designs can be attempted on the fly just by simply loading a different image onto the DMD chip. Further possible works include using these structures or other designs as master molds because DPPA can be chemically treated to include a releasing layer for mold detachment[28]. Microwells for single cell studies can also be performed with a variety of microwell sizes and geometries by changing the conditions and design used for printing.

Chapter 2, in part is currently being prepared for submission for publication. Y. Leong, S.C. Chen. This thesis author was the primary investigator and author of this material.

Chapter 3: 3D Printing Nanocomposites

3.1 3D-Printed Artificial Microfish

Aquatic organisms employ a variety of locomotive strategies to maneuver within their environments. Such mechanisms present a wide variety of inspirations in designing microswimmers for applications such as guided drug delivery to environmental decontamination[30–33]. A large problem when taking cues from biological designs for creating microswimmers, is to find a way to replicating the biological form and function. In this work, we use our μCOP system to: 3D print hydrogel microfishes with designed biomimetic structures, incorporate platinum (Pt) and magnetic (Fe_3O_4) nanoparticles for chemically and magnetically guided movement, as well as incorporate functionalized nanoparticles (PDA) for detoxification[34]. The speed of the microfishes can be tuned by changing the geometric design of the fish as well as by changing the concentration of the encapsulated Pt nanoparticles. This integration of multifunctional capabilities demonstrates the flexibility and potential for creating functional nanocomposites in a wide variety of applications such as actuation, sensing, and detoxifying.

Advances in nanotechnology as well as the methods for fabricating and manufacturing nanomaterials has presented the ability to create motors with biomimetic properties for self-propulsion[30–33]. Different methods for fabricating and manufacturing has led to the designs of multiple types of micro/nano swimmers with different locomotive techniques[35,36]. Methods to create rolled up nanostructures gave rise to tubular microjets as well as microdrillers[37–40]. Template-assisted

electrochemical deposition has been utilized to create tubular microrockets and nanomotors[41,42].

However, these methods only allow for manufacturing of simple geometries such as spheres or cylinder, restricting the ability to create complex and nuanced 3D designs that mimic biological functions. Additionally, such methods tend to only allow the use of homogenous inorganic materials, and as such, limits the multifunctional capabilities of the motors. Techniques that involve direct writing utilizing a laser have full capabilities of 3D designing complex structures with great specificity, such as helical structures that are inspired by bacterial flagella[43]. However, due to its serial nature, scaling up becomes an issue. Molding methods have also been employed for large batch fabrication of biomimetic micoswimmers made out of poly(dimethylsiloxane) (PDMS) powered by external magnetic fields or cardiomyocytes[44–46]. However, the magnetic materials and cells cannot be integrated into a single step during fabrication and manufacturing of the swimmer itself, limiting the addition of other functionalities as well as increasing the amount of time spent fabricating. A system that is capable of creating highly specified 3D structures with the ability to integrate different modes of multifunctionality with ease as well as possessing the potential for large batch fabrication is therefore a necessity to efficiently fabricate and manufacture more advanced microswimmers. The μCOP that we developed is fully capable of efficiently fulfilling these criteria's.

In this work, we used the μCOP system to fabricate artificial microfishes with biomimetic structures and guided movement capabilities, the μCOP system allows us

to design a wide variety of biomimetic structures due the digital nature of our computer aided system. We can easily load an image with designed biomimetic features and print them with high speeds and micron scale resolutions. In order to incorporate the guided movement functionality into the microfishes, we chose to make the fishes out of 700 Da poly(ethylene diacrylate) (PEGDA), purchased from Sigma-Aldrich, and functional nanoparticles. The microfishes are comprised mostly of PEGDA, a photopolymerizable polymer that is widely used for drug delivery and tissue scaffolds. PEGDA was also used to encapsulate both platinum (Pt) nanoparticles and magnetic (Fe_3O_4) nanoparticles to provide the chemical reaction for the microfishes' propulsion and to enable magnetic guidance. Additional detoxifying nanoparticles (PDA) were also encapsulated for toxin neutralization[34], showcasing the multifunctionality of the microfishes.

In order to optimize the microfishes swimming capability, we printed multiple biomimetic forms with different designs and sizes. A composition of 40 wt% PEGDA in water and 1 wt% lithium phenyl-2,4,6-trimethylbenzoylphosphinate as the photoinitiator[47] was used for the microfishes. Because of the fast and digital nature of the μCOP system, we can easily print wide arrays of fishes with different features and designs in <5s and cycle through multiple iterations in quick succession. SEM images of the printed microfishes are seen in **Figure 3.1.1 a-d**. **Figure 3.1.1 a** shows a single microfish with a measured height of 30μm and a length from head to tail of 200μm. **Figure 3.1.1 b** shows an of array of smaller printed microfishes with high uniformity and precision with lengths measuring 100μm. In a single array, we can also include microfishes with varying lengths ranging from 100μm up to 500μm, as seen in **Figure**

a)

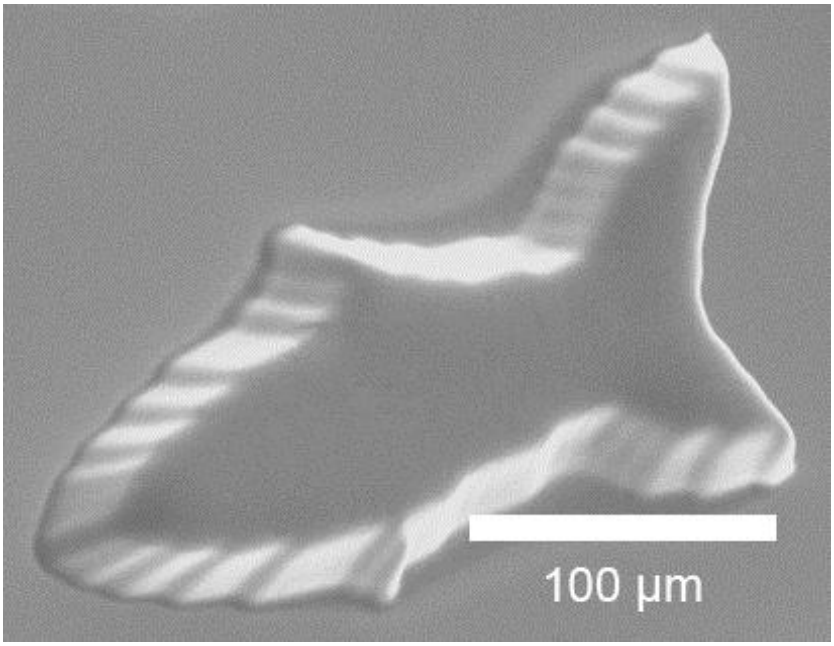

b)

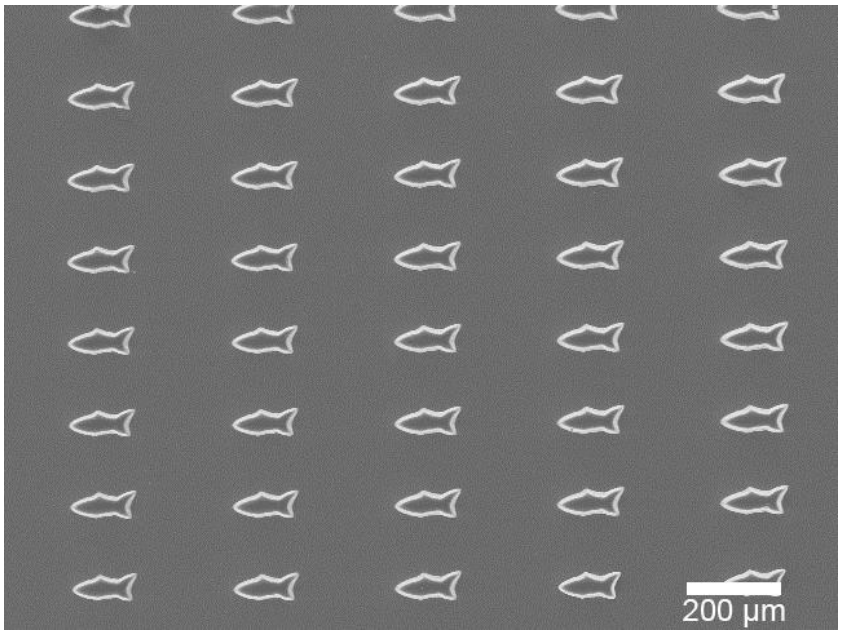

Figure 3.1.1: a) Single microfish that is 30µm in height with head to tail length of 200µm, b) Uniform array of smaller microfishes with head to tail length to 100µm

c)

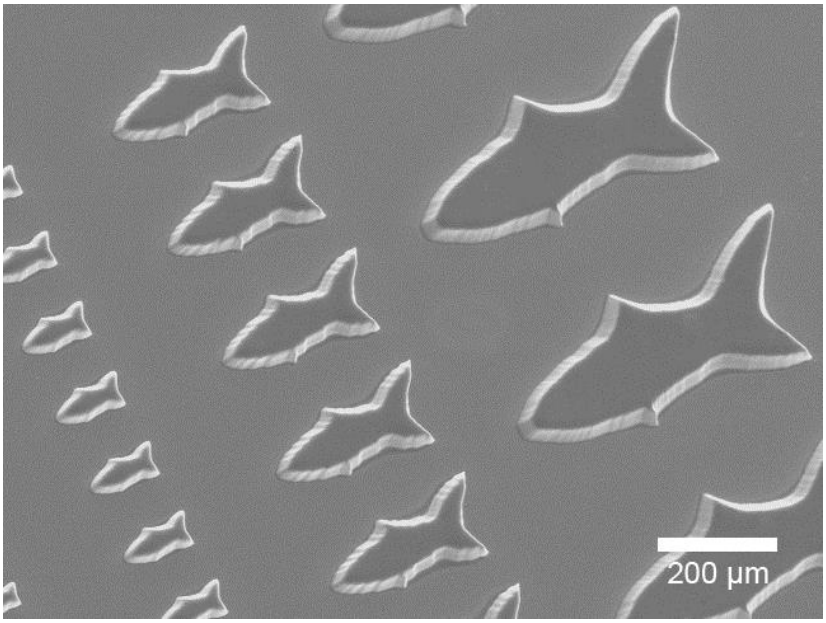

d)

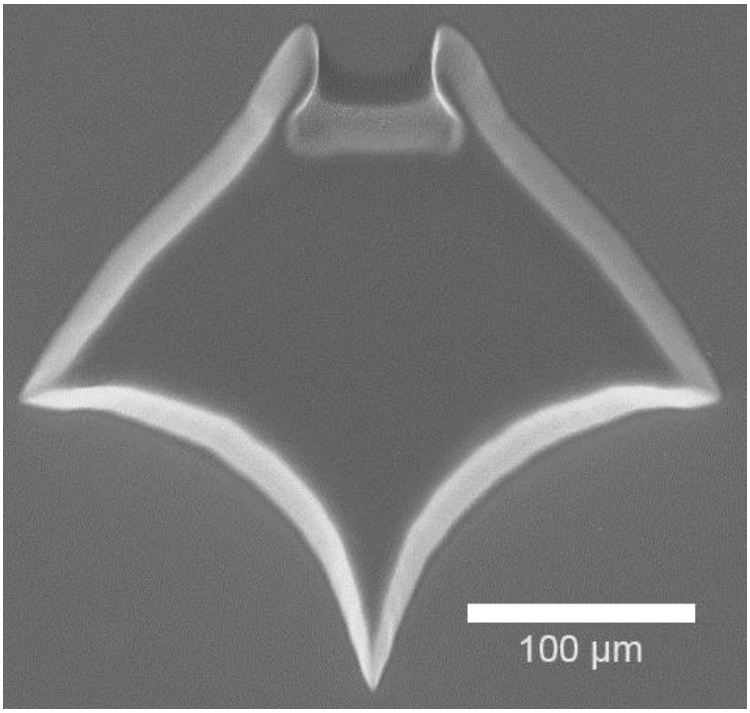

Figure 3.1.1: c) array of microfishes with varying lengths, d) Manta ray design, Continued.

3.1.1 c. We can also print different biomimetic designs, such as a manta ray inspired design, as seen in **Figures 3.1.1 d**.

Because of the high degree of spatial control that our μCOP system possess, we can spatially decide where to pattern or encapsulate different types of materials with great specificity for tunable multifunctional capabilities. For this work, we encapsulated Pt nanoparticles in the tail of the microfish and the magnetic nanoparticles in the head of the microfish, as seen in **Figure 3.1.2**. With these two nanoparticles and the ability to spatially encapsulate them, we were able to effectively control the swimming direction and speed of the printed microfishes. The printing and fabrication process of the microfishes with encapsulated nanoparticles is illustrated in **Figure 3.1.2 a**. First the entire body of the microfish was printed with the solution of PEGDA, next the remaining unpolymerized PEGDA solution was washed away and another solution of PEGDA containing dispersed Pt nanoparticles was flowed in. A second exposure for photopolymerization in the tail was performed to encapsulate the Pt nanoparticles. A concentration of $8.0 * 10^{8}$ particles/mL of Pt nanoparticles in the same PEGDA solution previously described was used. The Pt nanoparticles catalytically decomposes hydrogen peroxide into oxygen, which enables the microfish to propel itself. For the next step, the solution of PEGDA and Pt particles was thoroughly washed away and a solution of PEGDA and magnetic nanoparticles was then flowed in. A second exposure in the head was performed to encapsulate the Fe_3O_4 nanoparticles. A concentration of 5mg mL^{-1} of magnetic particles in the same PEGDA solution previously described was used. The magnetic nanoparticles allow the magnetic guidance of microfishes' movement. In order to confirm that the μCOP

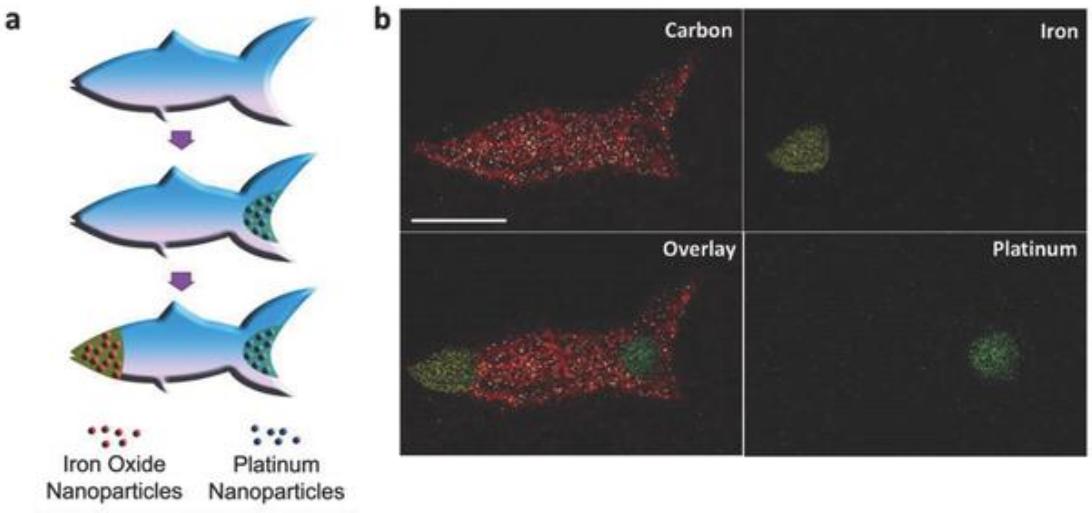

Figure 3.1.2: a) Printing and fabrication process of microfishes with encapsulated nanoparticles, b) EDX spectroscopy of microfishes with encapsulated nanoparticles

system can successfully spatially encapsulate the nanoparticles in the respective areas for the functionalization of the microfish, energy-dispersive X-ray (EDX) spectroscopy was performed. **Figure 3.1.2 b** confirms that the Pt nanoparticles are localized in the tail of the fish and that the magnetic nanoparticles are localized in the head of the fish. For increased functionality, additional nanoparticles can potentially be integrated into the microfishes, allowing for greater tunability.

The movement of the microfishes provided by the encapsulated Pt nanoparticles in hydrogen peroxide fuel can be seen in **Figures 3.1.3**. The bubbles of O_2 from the Pt assisted catalysis of hydrogen peroxide fuel provides the propulsion of the microfishes. The bubbles are created at a high frequency, providing smooth and continuous propulsion through the medium, displaying the catalytic efficiency of the spatially encapsulated Pt nanoparticles. Because propulsion is generated by the expulsion of O_2, the rate of catalytic decomposition is directly proportional to the propulsion speed[48]. Therefore, increasing the concentration of hydrogen peroxide and/or increasing the amount of Pt particles, will increase the rate of catalytic decomposition which leads to faster propulsion. In order to test this, concentrations of 5%, 10%, and 15% hydrogen peroxide were used. As seen in in **Figure 3.1.3 c**, the microfishes are faster in higher concentrations, with speeds up 780 $\mu m/s^{-1}$ in 15% hydrogen peroxide. The Stoke's drag force on the microfishes is directly related to the geometry and design of the microstructures[49]. Therefore, microfishes with different geometries will have different speeds even though they have the same Pt loading concentration while being fueled by the same concentration of hydrogen peroxide as well. The design seen in **Figure 3.1.3 a** represents the common fish design, denoted as

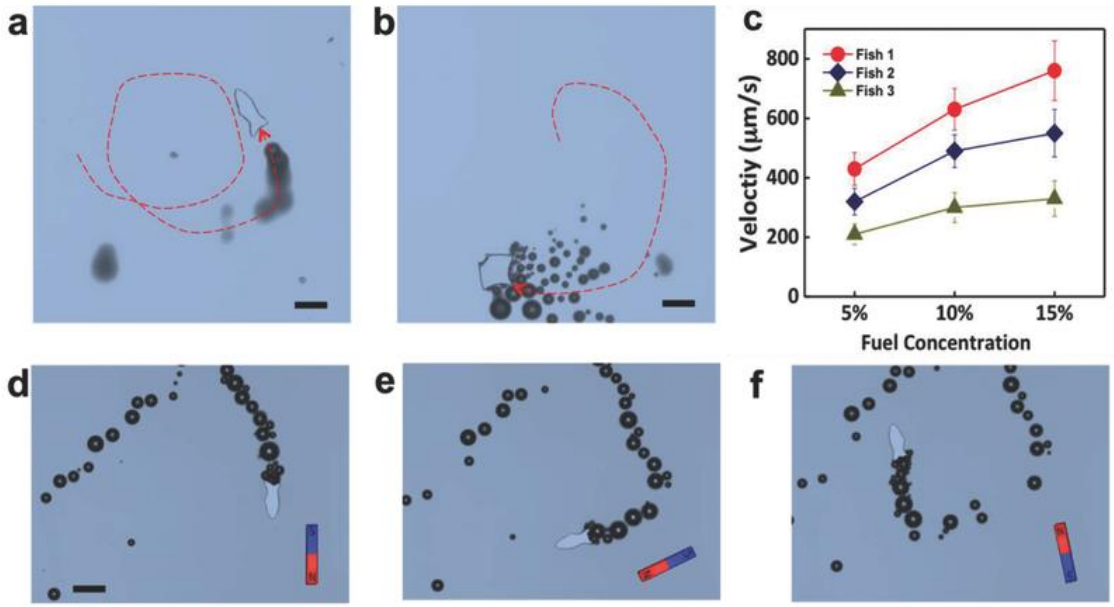

Figure 3.1.3: Images with motion tracking lines of a) common microfish, denoted fish 1, and b) manta ray microfish, denoted fish 2 in 10% hydrogen peroxide, c) Plot of different microfishes' speed in different concentrations of hydrogen peroxide, d-f) Sequentially taken pictures of a microfish guided by an external magnetic source

Fish 1, while the design seen in **Figure 3.1.3 b** represents the manta ray design, denoted as Fish 2. Comparing Fish 1 and Fish 2 in **Figure 3.1.3 c** clearly shows that Fish 1 is faster than Fish 2. This is due to the geometries of both fishes with Fish 1 experiencing lower drag forces compared to Fish 2. The average speed of Fish 1 is shown to be 1.5 times the average speed of Fish 2. From these results, it is clearly demonstrated that the speed of the microfishes can be finely tuned through optimizing the design and geometry of the fish. The ease of printing and as well as the flexibility of μCOP system can easily facilitate such optimizations of the microfishes. The speed of the microfishes is not limited to the design and geometry. As stated before, the rate of catalytic decomposition is directly proportional to the speed of the microfishes. By changing the concentration of encapsulated Pt nanoparticles, we can also tune the speed of the microfishes. A microfish, denoted as Fish 3, has the same design as Fish 1, but was instead loaded with a Pt nanoparticle concentration of 4.0 $*10^8$ particles/mL. This is half the concentration that was loaded into Fish 1. Fish 3 shows slower speeds than Fish 1 when fueled by the same concentrations of hydrogen peroxide, as seen in **Figure 3.1.3 c**. This confirms the ability to tune the speed of the microfishes by changing the loading concentration of Pt nanoparticles. Combined with the geometrical design as well as adjusting the loading concentration of Pt nanoparticles, we have a great control in tuning the speed of the microfishes through the μCOP system.

The magnetic nanoparticles that were spatially encapsulated in the head of the microfishes provide the ability to magnetically control the direction of microfishes movement. **Figures 3.1.3 d-f** show sequentially taken pictures of a microfish guided

by an external magnetic source. The microfish shows rapid alignment with the changing external magnetic field, allowing for fine control and easy changes in the direction of movement. Through the encapsulation of Pt nanoparticles and the magnetic nanoparticles, the microfishes show high degree of control and tunability of the speed as well as efficient control in guiding the microfishes and the capability to be applied in diverse applications.

In order to examine a possible application of the 3D-printed microfishes, detoxification nanoparticles, PDA, were additionally encapsulated into the body of the microfishes. PDA nanoparticles are made from the self-assembly of 10,12-pentacosodiynoic acid for the detoxification of melittin[34]. Encapsulated PDA nanoparticles in PEGDA have shown good detoxification properties in the previous work. When pore forming toxins, such as melittin, bind to the PDA nanoparticles, fluorescent emission occurs, allowing the use of fluorescence intensity as an indicator of detoxification efficiency in the experiment. The encapsulation of the PDA nanoparticles was performed with the same method as the encapsulation of the other nanoparticles, but here the PDA nanoparticles were spatially encapsulated in the entire body. A concentration of 3 mg mL^{-1} of PDA nanoparticles in the same PEGDA solution as described before was used. In order to examine the detoxification efficacy of the microfish, we had three testing conditions: a control, stationary microfishes, and mobile microfishes. Microfishes in all conditions were incubated in 5% hydrogen peroxide at 37^{o}C for 10 min. The control condition contained microfishes with encapsulated PDA and Pt nanoparticles placed in the solution of hydrogen peroxide with no melittin. No visible fluorescence was detected, as seen in **Figure 3.1.4 a**. The

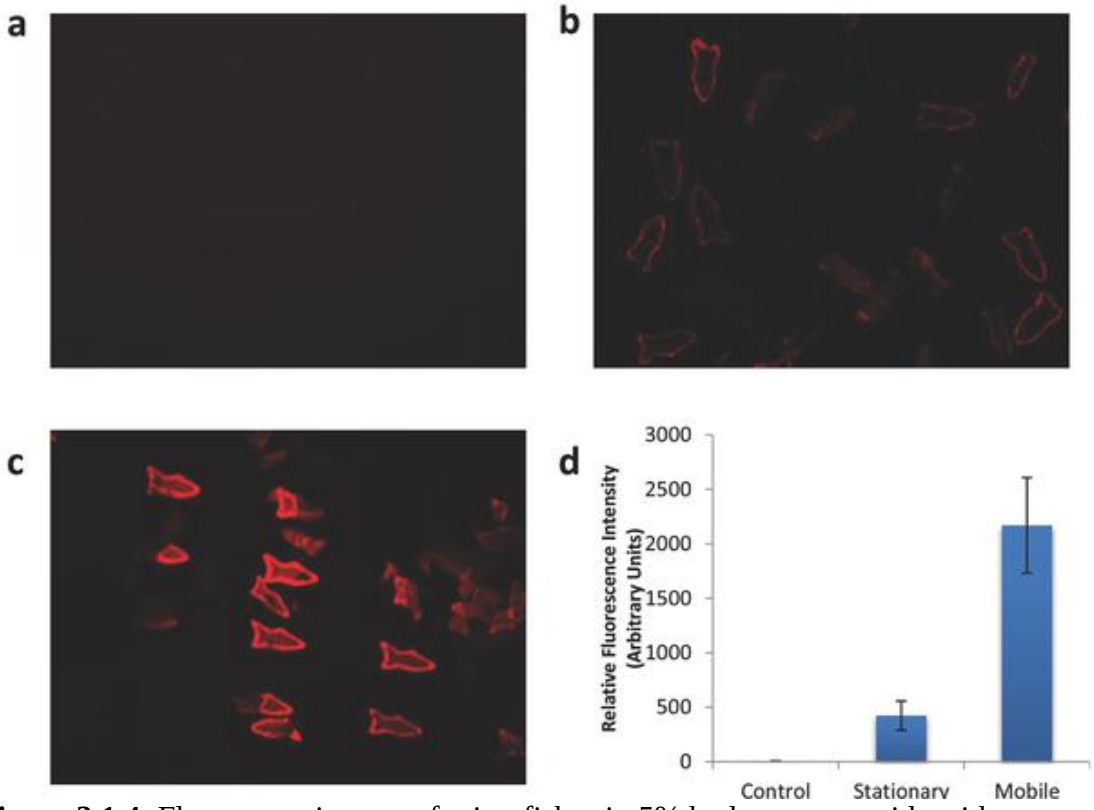

Figure 3.1.4: Fluorescent images of microfishes in 5% hydrogen peroxide with encapsulated PDA for detoxification of melittin. a) Control with PDA and Pt nanoparticles but no melittin, b) Stationary microfishes with PDA and melittin but no PT nanoparticles, c) Mobile microfishes with PDA, Pt nanoparticles, and melittin, d) Relative fluorescence intensity measurements indicating amount of melittin absorbed by the microfishes in each condition

stationary condition contained microfishes with encapsulated PDA, but no Pt nanoparticles, placed in the solution of hydrogen peroxide with 2.5 mg mL^{-1} melittin. Because there were no Pt particles, the microfishes were completely stationary during incubation. Low intensities of fluorescence were detected, as seen in **Figure 3.1.4 b**, confirming that the encapsulated PDA particles were interacting with the melittin. The mobile condition contained microfishes with encapsulated PDA and Pt nanoparticles placed in the solution of hydrogen peroxide with 2.5 mg mL^{-1} melittin. Because there were Pt nanoparticles, the fishes were moving during incubation. High intensities of fluorescence were detected, as seen in **Figure 3.1.4 c**, showing the impact of moving microfishes on the interaction between PDA and melittin. Further quantification of the fluorescence intensity was performed using ImageJ as previously described[50]. Relative fluorescence can be calculated according to **Equation 1**:

$$\text{Relative fluoresence intensity of fish} = \frac{\text{integrated intesnity of fish}}{\text{area of fish}} - \frac{\text{integrated intesnity of background}}{\text{area of background}} \quad (1)$$

The integrated intensity and area can be measured directly using ImageJ. The data from all three conditions are plotted in **Figure 3.1.4 d**. Statistical analysis was performed to compare the means of the conditions through the use of analysis of variance (ANOVA) followed by Tukey's post-hoc test. $p < 0.05$ was considered statistically significant. From the data, it is shown that moving microfishes are significantly more efficient in detoxifying compared to stationary microfishes, exemplifying how important movement is in removing toxins.

In this work we showed the ability to rapidly 3D print microfishes with designed biomimetic features using the μCOP system with in a parallel manner. By

altering the geometrical design, we can tune the speed of the microfishes to the desired speed for any application. The μCOP can easily facilitate the speed optimization of any microfish through the ability to load any design on the fly as well as the ability to print microfishes in mere seconds. We also displayed the ability to spatially encapsulate nanoparticles for multifunctional capabilities with a great deal of control and precision. Pt nanoparticles were encapsulated for locomotive purposes by catalytically decomposing hydrogen peroxide to produce oxygen gas for propulsion. Magnetic nanoparticles were encapsulated to provide the ability to magnetically guide the direction of the microfishes. Detoxifying PDA nanoparticles were additionally encapsulated in the microfishes for toxin detoxification. It was shown that the microfishes were more efficient in interacting with the toxins when they were moving, showcasing a possible detoxifying application with the microfishes. We are not limited by the nanoparticles that were mentioned in this work. This work can be further expanded to include other components such as Ag, Ir, MnO_2, or catalases to interact with different types of fuel[51,52]. There have been works with micromotors to use water as a source of fuel instead[53,54], which could possibly be integrated into future works with the microfishes to improve its potential to be used in highly practical applications. Different functional nanoparticles, other than PDA, can be added for greater multifunctionality. Our system can potentially be applied and tuned for applications such as drug delivery and environmental remediation.

3.2 3D printable, Bisphenol A-free, Piezoelectric Polycarbonate Nanocomposite

Piezoelectricity allows for the conversion of mechanical forces into electrical energy and vice versa. Piezoelectric nanocomposites provide the ability to create smaller functional piezoelectric devices while helping mitigate undesirable mechanical properties that piezoelectric materials might possess such as brittleness. Because the polymer imparts its mechanical properties on the nanocomposite, polymer choice is very important. Polycarbonate is a widely used polymer due to its desirable mechanical properties such as high toughness and impact strength, but current processing methods are not suited for 3D printing. Additionally, current techniques used to create nanocomposites do not have capabilities to easily fabricate 3D structures and designs on the nano/micron scale. In this current work in progress, we present the use of TPP to 3D print highly defined piezoelectric nanocomposites using 20nm $BaTiO_3$ (BTO) nanoparticles and a bisphenol-A (BPA) free photopolymerizable polycarbonate (PC). The printed structures display high uniformity across all printed areas with resolutions down to 1-2μm. The BTO nanoparticles in the nanocomposites does not interfere with the printing capabilities of the TPP system allowing the system to retain its high precision capabilities. Having the ability to 3D print piezoelectric composites with high resolutions and precision opens many possibilities to create devices that require intricate 3D geometries and design. BTO surface modification must be investigated along with additional mechanical characterization of PC and piezoelectric characterization of BTO-PC composite before this work can be concluded.

Piezoelectricity is a phenomenon in which a dielectric material generates electrical surface charge in response to mechanical strain, or vice versa[55]. This is due to the deformation of the material's non-centrosymmetric unit cell, inducing an internal polarization on the unit cell. Such properties have been used to create nano resolution stages[56] and ultrasound transducers[57]. Most of these applications uses ceramic based materials due to its strong piezoelectric properties. However, piezoelectric ceramics have limitations such as being brittle which limits its flexible applications. Furthermore, highly piezoelectric ceramics, such as lead zirconate titanate, can contain toxic elements which limits its use in biological systems. Studies on piezoelectric polymers such as polyvinylidene fluoride (PVDF) have been done to try and overcome these issues, but PVDF has relatively low piezoelectric coefficient of <25 pC/N[58], whereas PZT has a piezoelectric coefficient of >250pC/N[59] depending on composition. In order to overcome the natural brittleness of piezoelectric ceramics while still maintaining good piezoelectric properties, piezoelectric polymer composites have been studied and have been used to improve devices such as ultrasound transducers[57,60,61]. Polymer composites provide better mechanical properties such as increased flexibility, while still being able to maintain its good piezoelectric properties. Recently in the last few years, advances in piezoelectric nanocomposites have been made. Some works include the use of $ZnSnO_3$-PDMS nanocomposites for high-power generation with a large output voltage of 20V[62] and a highly flexible ZnO nanowire-PMMA nanocomposite for energy harvesting and deformation sensing[63]. The processes used to fabricate these devices do not provide the ability to easily fabricate 3D structures and designs. Any sort of multilayered designs would require

multiple processing steps. Providing the ability to fabricate intricate 3D geometries in a simple, singular process can open up many possibilities for designing devices that require complicated geometries.

In a previous work, the μCOP system was used to 3D print 80nm $BaTiO_3$-PEGDA nanocomposites[64], providing an alternate solution to these issues. The printed structures were 100μm-200μm in size with reported resolutions down to ~5μm. Although the μCOP system can print large arrays, it does not have the ability to print smaller and finer structures with defined 3D features and details with <5μm resolutions. $BaTiO_3$ (BTO) used in the previous work is a lead-free alternative to PZT with bulk piezoelectric coefficient of >190 pC/N[65,66], depending on synthesis and processing. It was also reported in the work that smaller BTO nanoparticles could improve the optical transparency of the printed structures, potentially allowing for greater the mass loading. Additionally, PEGDA that was used in the previous work does not provide high durability and mechanical stiffness that might be desired for certain applications. In light of these issues, we present the ability and use of TPP to 3D print highly defined piezoelectric nanocomposites structures with 1-2μm resolutions using 20nm BTO nanoparticles and bisphenol-A (BPA) free photopolymerizable polycarbonate (PC).

Polycarbonate is a widely used polymer in automotive parts, building and construction, data storage on CDs[67], and recently has found use for biomedical applications as well as tissue engineering scaffolds[68]. PC possess desirable mechanical properties such as its high toughness and impact strength. However, one of its largest

drawbacks is that PC commonly made out of the polymerization of BPA and phosgene. BPA is an estrogen analog that has been under scrutiny for possibly causing human developmental problems in children[69,70]. Therefore, exploring and finding a BPA-free PC is highly desirable especially in products that come in direct contact with humans such as children toys, medicine, and foods. One of the most promising methods of creating BPA-free PC is through ring opening polymerization (ROP) of cyclic monomers to form aliphatic PC[68]. Recently a synthetic facile and green route with scalable capabilities of six-membered functional cyclic carbonates have been reported[71–73]. Such monomers also present the ability to functionalize side groups for additional material properties, such as the ability to make it photopolymerizable. No photopolymerizable PC has been reported thus far and the ability to do so opens up new possibilities to use PC, especially for optical 3D printing methods. In this work, we report a two-step polymerization process to create a photopolymerizable PC. The two-step polymerization process is shown in **Figure 3.2.1**. The first step involves the thermal ROP of methacrylated trimethylolpropane cyclic carbonate (TMPMAC) and unfunctionalized trimethylolpropane cyclic carbonate (TMPC) to create random copolycarbonate. The second step involves photpolymerization to cross-link the methacrylate groups in the random copolycarbonate. Using TPP to 3D print PC-BTO nanocomposites, we can fabricate piezoelectric devices for use in areas such as micro electromechanical systems (MEMS), power generation and harvesting, mechanical force sensing, or for biomedical applications.

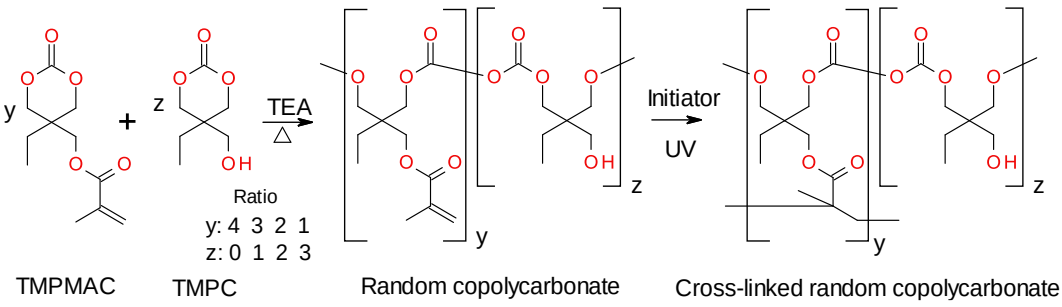

Figure 3.2.1: The two step polymerization process of BPA-free photopolymerizable PC. First step involves ROP of TMPMAC and TMC. Second step is the photopolymerization to cross link methacrylate groups

TMPMAC and TMPC were provided by Cyclicor AB (Sweden), triethylamine and 1-propanol were purchased from Sigma-Aldrich, and Irgacure-819 was purchased from Ciba Inc. 20 nm BTO nanoparticles were prepared as described in another work[74]. To prepare the photopolymerizable PC, TMPMAC and TMPC can be mixed in varying molar ratios. By changing the ratios of TMPMAC and TMPC relative to each other, the crosslinking densities can be tuned to give different mechanical properties. Due to this work still being in progress at the time of writing and to simplify the results, a molar ratio of 2:2 was used. This corresponds to a 0.2 mmol of TMPMAC (45.6mg) and 0.2 mmol of TMPC (32.4 mg). The two monomers were placed in a 1.5 mL Eppendorf tube with 3µL of triethylamine and 3µL 1-propanol. The mixture was heated and mixed at 90^{o}C for 5 minutes. For samples without BTO, 4.5 µL of 5% wt/vol of Irgacure 819 in ethanol was added. For samples with BTO, 1 wt% of BTO nanoparticles was additionally. The solution was then heated and mixed for another 1 minute and was used immediately after heating. After printing with TPP, the polymerized structures were thoroughly washed with ethanol to remove all unpolymerized polymer from the structures.

To demonstrate the ability to print PC first, we dispense 3 µL of the PC solution without any BTO nanoparticles onto the glass substrate for TPP. The laser power was set to 120 mW using a laser beam attenuator and the writing speed was set to 60 µm/s. SEM images of simple structures such as tessellated hourglass geometries are shown in **Figures 3.2.2 a,b**. The structures printed using TPP show high uniformity across all printed areas, displaying the high precision and definition that the TPP system possess. The line width of the structures is measured to be 2µm. This can

a)

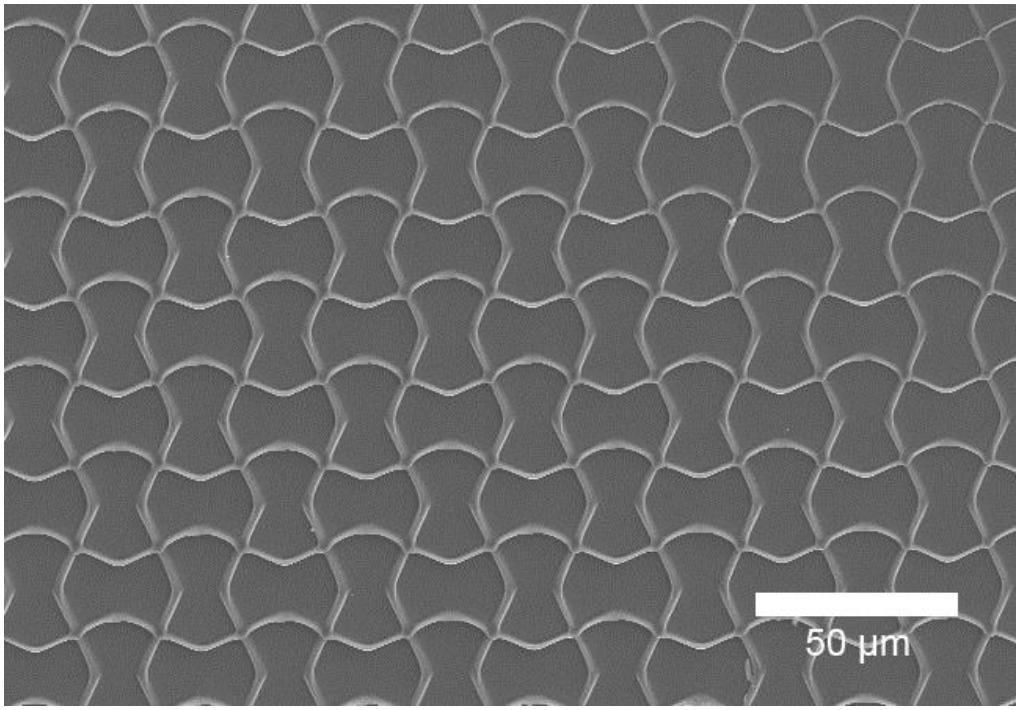

b)

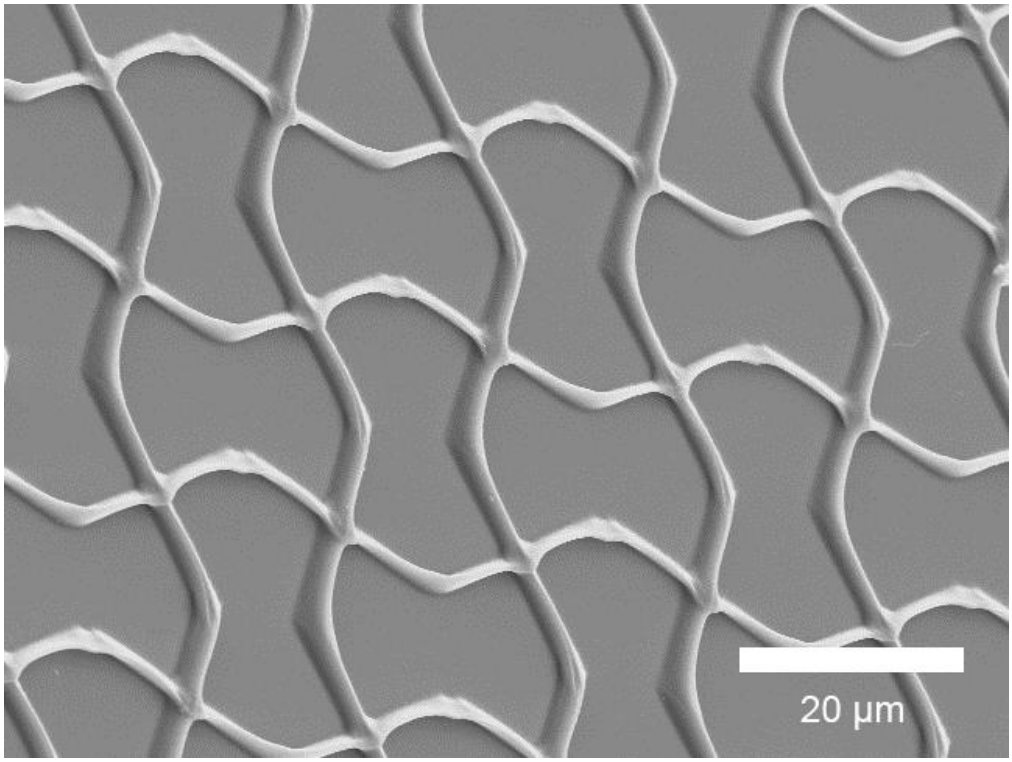

Figure 3.2.2: 3D printed tessellated hourglass geometries of pure PC using TPP, a) top-down view, b) tilted view

easily be tuned to any desired width by changing the power or the write speed of the TPP process. The power is directly proportional to the line width while the write speed is inversely proportional to the line width. The height of the structure was measured to be approximately 3μm tall. The height of the structure can easily be increased by using TPP to polymerize another layer on top, allowing for precise 3D multilayer designs in a single processing step. With these abilities at hand, we can easily tune the geometrical specificities and design. Next, we demonstrate the ability to 3D print BTO-PC nanocomposite by including 20nm BTO nanoparticles into the photopolymerizable PC. 3 μL of the BTO-PC solution was dispensed onto the glass substrate and the laser power was set to 135 mW and writing speed was set to 60 μm/s. A single layer printed grid is shown in **Figure 3.2.3 a**. Just like the pure PC, the structure shows high uniformity across the printed areas. The line width was measured to be 1.8μm with measured height of the structure to be approximately 3μm tall. A multilayer printed grid is shown in **Figure 3.2.3 b**. This was done by polymerizing multiple layers on top one another. The laser power and writing speed was the same as the single layer grid. The line width was measured to be 2.2μm with measured height of the structure to be approximately 10μm. Higher magnification images of the printed structures' surfaces of both pure PC and BTO-PC are shown in **Figures 3.2.4 a** and **b** respectively. The BTO-PC surface is significantly rougher with aggregate particles protruding from the surface of the polymer when compared to the much smoother pure PC surface. This confirms the presence of BTO nanoparticles in the BTO-PC nanocomposite. Although the BTO nanoparticles are 20 nm in size, they form clearly visible aggregates in the BTO-PC nanocomposite. The sizes of these aggregates are

a)

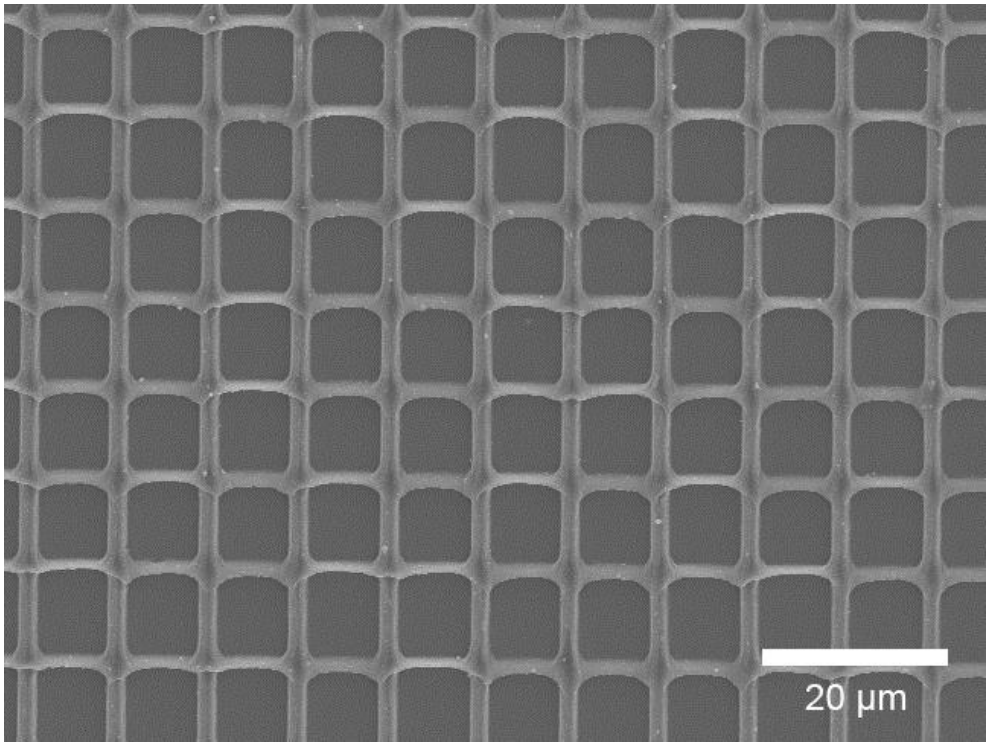

b)

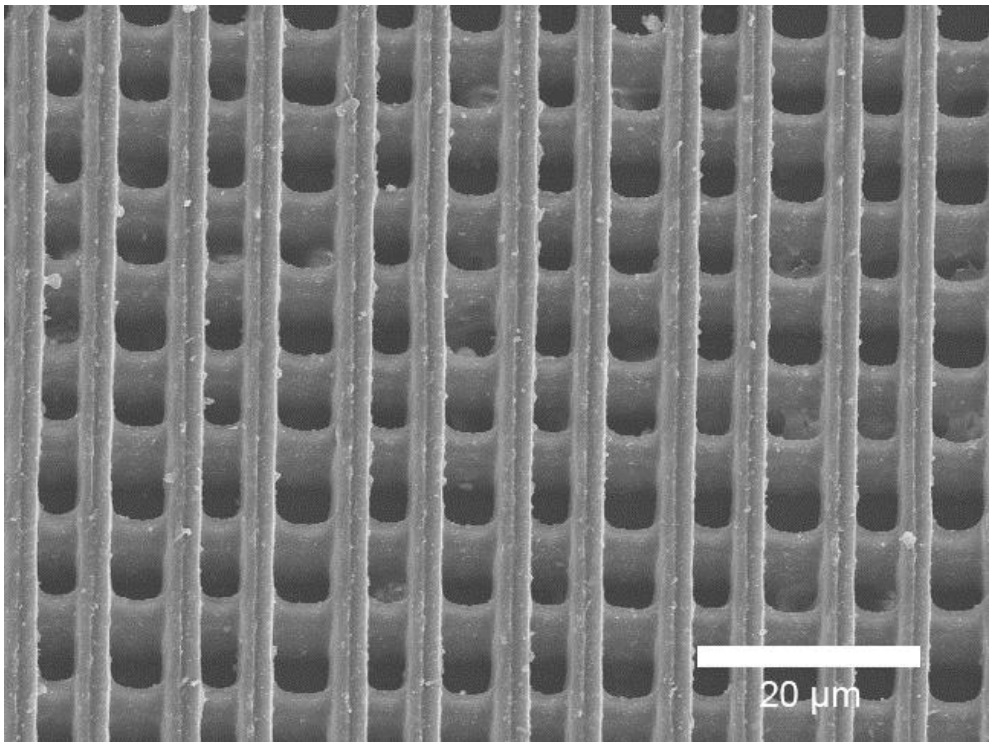

Figure 3.2.3: 3D printed BTO-PC nanocomposite using TPP, a) a single layer grid, b) a multilayer grid

a)

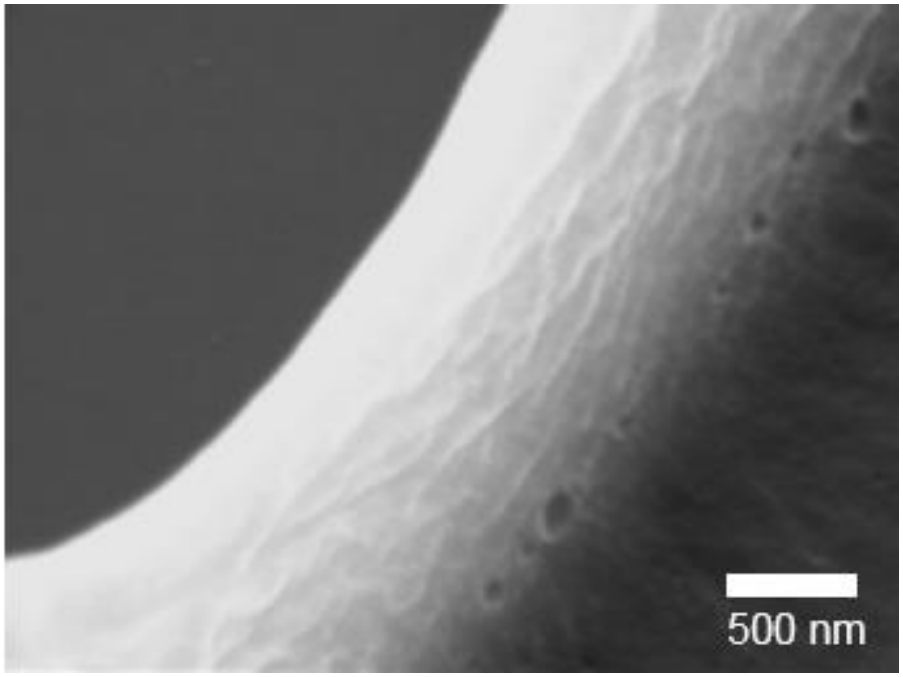

b)

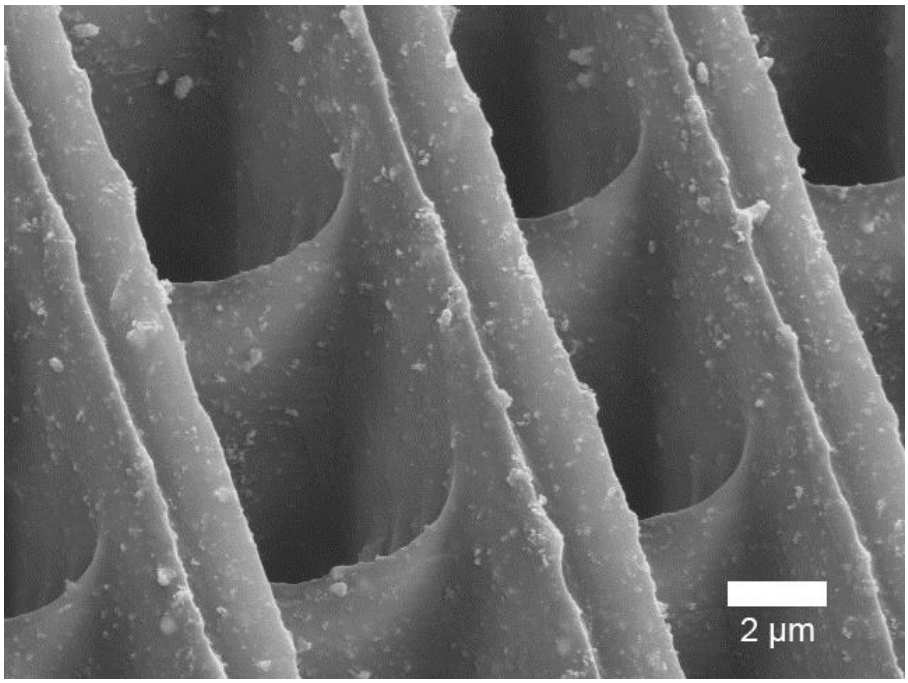

Figure 3.2.4: Higher magnification images of the 3D printed surfaces, a) pure PC, b) BTO-PC nanocomposite

highly varied, ranging from 50nm to 400nm. Even though the BTO-PC nanocomposite contain nanoparticles which could negatively affect the TPP printing abilities by interacting with the laser light, the same high level of uniformity, precision and definition of TPP printing is retained when compared to the printed structures of pure PC. This indicates that the nanoparticles do not hinder the TPP's ability to 3D print nanocomposite structures.

In conclusion, we display the ability to print BTO-PC nanocomposites using TPP. Photopolymerizable PC was made possible through a two-step polymerization process: ROP of cyclic carbonates with methacrylate functional groups, followed by photopolymerization to cross link the polymer. We can achieve high structure uniformity across printed areas as well as high precision printing and definition with the TPP system. These desirable properties are not diminished when printing BTO-PC compared to pure PC. Because this work is still in progress at the time of writing, additional work to characterize the mechanical properties of differing molar ratios of PC will be done. Piezoelectric characterization of the BTO-PC composite will also be performed to confirm its piezoelectric properties. The printability of the other molar ratios of PC and BTO-PC must be examined due to differing crosslinking densities each ratio produces. In the previous μCOP work with BTO-PEGDA, it was shown that surface modification of the 80nm BTO nanoparticles affects the piezoelectric coefficient. Therefore, a similar study into surface modifications of the 20nm BTO is required to examine the effects on piezoelectricity. Future possible applications of BTO-PC nanocomposite include the fabrication of a working device utilizing its

piezoelectric properties. Such applications could involve 3D printing arrays of tunable ultrasound transducers[75] or 3D printing electroactive tissue scaffolds[76].

Section 3.1, in part, is a reprint of the material as it appears in Zhu, W., Li, J., Leong, Y., Rozen, I., Qu, X., Dong, R., Wu, Z., Gao, W., Chung, P., Wang, J. & Chen, S. 3D-Printed Artificial Microfish. *Adv. Mater.* **27**, 4411-4417 (2015). The thesis author was the third author of this paper.

Section 3.2, in part, is currently being prepared for submission for publication of the material. Leong, Y., Chen, S. This thesis author was the primary investigator and author of this material.

Chapter 4: Conclusion and Future Works

In this thesis, we have shown the ability to 3D print functional nanocomposites using both the μCOP system and TPP system. With the μCOP system, we 3D printed artificial microfishes with encapsulated nanoparticles for multifunctional purposes. Pt nanoparticles provided the propulsion by catalytically decomposing hydrogen peroxide into oxygen. Magnetic nanoparticles provided the ability to magnetically guide the microfishes using an external magnetic source. The speed of the microfishes can additionally be tuned to any desired speed by changing the geometric design of the fish as well as by changing the concentration of the encapsulated Pt nanoparticles. Additional multifunctionality can be added onto the microfishes through the ability to spatially decide where to encapsulate nanoparticles and this was shown by the addition of detoxifying PDA nanoparticles. PDA nanoparticles were encapsulated onto the body of the microfishes and displayed detoxification capabilities. Additionally, significantly increased detoxification was found in mobile microfishes with Pt encapsulated nanoparticles compared to stationary microfishes with no Pt nanoparticles. Future possible works on the microfishes include the expansion to encapsulate other nanoparticles for additional functionality. Nanoparticles that can interact with other types of fuel such as water could enable the use of the microfishes in broader applications. Different types functional nanoparticles besides PDA can encapsulated into the microfishes as well.

Using the TPP system, we were able to 3D print BTO-PC nanocomposites using TPP. Photopolymerizable PC was made possible through a two-step

polymerization process: ROP of cyclic carbonates followed by photopolymerization to 3D print highly defined piezoelectric nanocomposites using 20nm $BaTiO_3$ (BTO) nanoparticles and a bisphenol-A (BPA) free photopolymerizable polycarbonate (PC). The printed structures display high uniformity across all printed areas with resolutions down to 1-2µm. The BTO nanoparticles in the nanocomposites does not interfere with the printing capabilities of the TPP system allowing the system to retain its high precision capabilities. Having the ability to 3D print piezoelectric composites with high resolutions and precision opens many possibilities to create devices that require intricate 3D geometries and design. BTO surface modification must be investigated along with additional mechanical characterization of PC and piezoelectric characterization of BTO-PC composite before this work can be concluded.

References

(1) Gu, D. D.; Meiners, W.; Wissenbach, K.; Poprawe, R. Laser Additive Manufacturing of Metallic Components: Materials, Processes and Mechanisms. *Int. Mater. Rev.* **2012**, *57*, 133–164.

(2) Derby, B. Printing and Prototyping of Tissues and Scaffolds. *Science (80-.).* **2012**, *338*, 921–926.

(3) Zhang, X.; Jiang, X. N.; Sun, C. Micro-Stereolithography of Polymeric and Ceramic Microstructures. *Sensors Actuators, A Phys.* **1999**, *77*, 149–156.

(4) Hong, S.; Yeo, J.; Kim, G.; Kim, D.; Lee, H.; Kwon, J.; Lee, H.; Lee, P.; Ko, S. H. Nonvacuum, Maskless Fabrication of a Flexible Metal Grid Transparent Conductor by Low-Temperature Selective Laser Sintering of Nanoparticle Ink. *ACS Nano* **2013**, *7*, 5024–5031.

(5) Paul, D. R.; Robeson, L. M. Polymer Nanotechnology: Nanocomposites. *Polymer (Guildf).* **2008**, *49*, 3187–3204.

(6) Croce, F.; Appetecchi, G. B.; Persi, L.; Scrosati, B. Nanocomposite Polymer Electrolytes for Lithium Batteries. *Nature* **1998**, *394*, 456–458.

(7) Ramanathan, T.; Abdala, A. A.; Stankovich, S.; Dikin, D. A.; Herrera-Alonso, M.; Piner, R. D.; Adamson, D. H.; Schniepp, H. C.; Chen, X.; Ruoff, R. S.; *et al.* Functionalized Graphene Sheets for Polymer Nanocomposites. *Nat. Nanotechnol.* **2008**, *3*, 327–331.

(8) Podsiadlo, P.; Kaushik, A. K.; Arruda, E. M.; Waas, A. M.; Shim, B. S.; Xu, J.; Nandivada, H.; Pumplin, B. G.; Lahann, J.; Ramamoorthy, A.; *et al.* Ultrastrong and Stiff Layered Polymer Nanocomposites. *Science* **2007**, *318*, 1–4.

(9) Xing, J.-F.; Zheng, M.-L.; Duan, X.-M. Two-Photon Polymerization Microfabrication of Hydrogels: An Advanced 3D Printing Technology for Tissue Engineering and Drug Delivery. *Chem. Soc. Rev.* **2015**, *44*, 5031–5039.

(10) Liu, J.; Hwang, H. H.; Wang, P.; Whang, G.; Chen, S. C. Direct 3D Printing of Cell-Laden Constructs in Microfluidic Architectures. *Lab Chip* **2016**, *16*, 1430–1438

(11) Ma, X.; Qu, X.; Zhu, W.; Li, Y.-S.; Yuan, S.; Zhang, H.; Liu, J.; Wang, P.; Lai, C. S. E.; Zanella, F.; *et al.* Deterministically Patterned Biomimetic Human iPSC-Derived Hepatic Model via Rapid 3D Bioprinting. *Proc. Natl. Acad. Sci.* **2016**, 201524510.

(12) Zhu, W.; Li, J.; Leong, Y. J.; Rozen, I.; Qu, X.; Dong, R.; Wu, Z.; Gao, W.; Chung, P. H.; Wang, J.; *et al.* 3D-Printed Artificial Microfish. *Adv. Mater.* **2015**, *27*, 4411–4417.

(13) Zhang, A. P.; Qu, X.; Soman, P.; Hribar, K. C.; Lee, J. W.; Chen, S.; He, S. Rapid Fabrication of Complex 3D Extracellular Microenvironments by

Dynamic Optical Projection Stereolithography. *Adv. Mater.* **2012**, *24*, 4266–4270.

(14) Soman, P.; Chung, P. H.; Zhang, A. P.; Chen, S. Digital Microfabrication of User-Defined 3D Microstructures in Cell-Laden Hydrogels. *Biotechnol. Bioeng.* **2013**, *110*, 3038–3047.

(15) Park, S. H.; Yang, D. Y.; Lee, K. S. Two-Photon Stereolithography for Realizing Ultraprecise Three-Dimensional Nano/microdevices. *Laser Photonics Rev.* **2009**, *3*, 1–11.

(16) Ovsianikov, A.; Viertl, J.; Chichkov, B.; Oubaha, M.; MacCraith, B.; Sakellari, I.; Giakoumaki, A.; Gray, D.; Vamvakaki, M.; Farsari, M.; *et al.* Ultra-Low Shrinkage Hybrid Photosensitive Material for Two-Photon Polymerization Microfabrication. *ACS Nano* **2008**, *2*, 2257–2262.

(17) Tayalia, P.; Mendonca, C. R.; Baldacchini, T.; Mooney, D. J.; Mazur, E. 3D Cell-Migration Studies Using Two-Photon Engineered Polymer Scaffolds. *Adv. Mater.* **2008**, *20*, 4494–4498.

(18) Sinha Ray, S.; Okamoto, M. Polymer/layered Silicate Nanocomposites: A Review from Preparation to Processing. *Prog. Polym. Sci.* **2003**, *28*, 1539–1641.

(19) Gullapalli, H.; Vemuru, V. S. M.; Kumar, A.; Botello-Mendez, A.; Vajtai, R.; Terrones, M.; Nagarajaiah, S.; Ajayan, P. M. Flexible Piezoelectric ZnO-Paper Nanocomposite Strain Sensor. *Small* **2010**, *6*, 1641–1646.

(20) Postiglione, G.; Natale, G.; Griffini, G.; Levi, M.; Turri, S. Conductive 3D Microstructures by Direct 3D Printing of Polymer/carbon Nanotube Nanocomposites via Liquid Deposition Modeling. *Compos. Part A Appl. Sci. Manuf.* **2015**, *76*, 110–114.

(21) Guo, S.-Z.; Yang, X.; Heuzey, M.-C.; Therriault, D. 3D Printing of a Multifunctional Nanocomposite Helical Liquid Sensor. *Nanoscale* **2015**, *7*, 6451–6456.

(22) Chiappone, A.; Fantino, E.; Roppolo, I.; Lorusso, M.; Manfredi, D.; Fino, P.; Pirri, C. F.; Calignano, F. 3D Printed PEG-Based Hybrid Nanocomposites Obtained by Sol-Gel Technique. *ACS Appl. Mater. Interfaces* **2016**, acsami.5b12578.

(23) Campbell, T. A.; Ivanova, O. S. 3D Printing of Multifunctional Nanocomposites. *Nano Today* **2013**, *8*, 119–120.

(24) Kwon, I. K.; Matsuda, T. Photo-Polymerized Microarchitectural Constructs Prepared by Microstereolithography (μSL) Using Liquid Acrylate-End-Capped Trimethylene Carbonate-Based Prepolymers. *Biomaterials* **2005**, *26*, 1675–1684.

(25) Lindstrom, S.; Andersson-Svahn, H. Overview of Single-Cell Analyses: Microdevices and Applications. *Lab Chip* **2010**, *10*, 3363–3372.

(26) Moeller, H. C.; Mian, M. K.; Shrivastava, S.; Chung, B. G.; Khademhosseini, A. A Microwell Array System for Stem Cell Culture. *Biomaterials* **2008**, *29*, 752–763.

(27) Rettig, J. R.; Folch, A. Large-Scale Single-Cell Trapping and Imaging Using Microwell Arrays. *Anal. Chem.* **2005**, *77*, 5628–5634.

(28) Zhang, W.; Han, L.-H.; Chen, S. Integrated Two-Photon Polymerization With Nanoimprinting for Direct Digital Nanomanufacturing. *J. Manuf. Sci. Eng.* **2010**, *132*, 030907.

(29) Sun, C.; Fang, N.; Wu, D. M.; Zhang, X. Projection Micro-Stereolithography Using Digital Micro-Mirror Dynamic Mask. *Sensors Actuators, A Phys.* **2005**, *121*, 113–120.

(30) Ismagilov, R. F.; Schwartz, A.; Bowden, N.; Whitesides, G. M. Autonomous Movement and Self-Assembly. *Angew. Chemie - Int. Ed.* **2002**, *41*, 652–654.

(31) Wang, J.; Manesh, K. M. Motion Control at the Nanoscale. *Small* **2010**, *6*, 338–345.

(32) Ozin, G. A.; Manners, I.; Fournier-Bidoz, S.; Arsenault, A. Dream Nanomachines. *Adv. Mater.* **2005**, *17*, 3011–3018.

(33) Mei, Y.; Solovev, A. A.; Sanchez, S.; Schmidt, O. G. Rolled-up Nanotech on Polymers: From Basic Perception to Self-Propelled Catalytic Microengines. *Chem. Soc. Rev.* **2011**, *40*, 2109–2119.

(34) Gou, M.; Qu, X.; Zhu, W.; Xiang, M.; Yang, J.; Zhang, K.; Wei, Y.; Chen, S. Bio-Inspired Detoxification Using 3D-Printed Hydrogel Nanocomposites. *Nat. Commun.* **2014**, *5*, 3774.

(35) Fischer, P.; Ghosh, A. Magnetically Actuated Propulsion at Low Reynolds Numbers: Towards Nanoscale Control. *Nanoscale* **2011**, *3*, 557–563.

(36) Wang, J.; Gao, W. Nano/Microscale Motors: Biomedical Opportunities and Challenges. *ACS Nano* **2012**, *6*, 5745–5751.

(37) Balasubramanian, S.; Kagan, D.; Jack Hu, C. M.; Campuzano, S.; Lobo-Casta??on, M. J.; Lim, N.; Kang, D. Y.; Zimmerman, M.; Zhang, L.; Wang, J. Micromachine-Enabled Capture and Isolation of Cancer Cells in Complex Media. *Angew. Chemie - Int. Ed.* **2011**, *50*, 4161–4164.

(38) Mei, Y.; Huang, G.; Solovev, A. A.; Ureña, E. B.; Mönch, I.; Ding, F.; Reindl, T.; Fu, R. K. Y.; Chu, P. K.; Schmidt, O. G. Versatile Approach for Integrative and Functionalized Tubes by Strain Engineering of Nanomembranes on Polymers. *Adv. Mater.* **2008**, *20*, 4085–4090.

(39) Solovev, A. A.; Mei, Y.; Ureña, E. B.; Huang, G.; Schmidt, O. G. Catalytic Microtubular Jet Engines Self-Propelled by Accumulated Gas Bubbles. *Small* **2009**, *5*, 1688–1692.

(40) Solovev, A. A.; Xi, W.; Gracias, D. H.; Harazim, S. M.; Deneke, C.; Sanchez,

S.; Schmidt, O. G. Self-Propelled Nanotools. *ACS Nano* **2012**, *6*, 1751–1756.

(41) Paxton, W. F.; Kistler, K. C.; Olmeda, C. C.; Sen, A.; St Angelo, S. K.; Cao, Y.; Mallouk, T. E.; Lammert, P. E.; Crespi, V. H. Catalytic Nanomotors: Autonomous Movement of Striped Nanorods. *J. Am. Chem. Soc.* **2004**, *126*, 13424–13431.

(42) Gao, W.; Dong, R.; Thamphiwatana, S.; Li, J.; Gao, W.; Zhang, L.; Wang, J. Artificial Micromotors in the Mouse's Stomach: A Step toward in Vivo Use of Synthetic Motors. *ACS Nano* **2015**, *9*, 117–123.

(43) Tottori, S.; Zhang, L.; Qiu, F.; Krawczyk, K. K.; Franco-Obregón, A.; Nelson, B. J. Magnetic Helical Micromachines: Fabrication, Controlled Swimming, and Cargo Transport. *Adv. Mater.* **2012**, *24*, 811–816.

(44) Stanton, M. M.; Trichet-Paredes, C.; Sánchez, S.; Khalil, I. S. M.; Dijkslag, H. C.; Abelmann, L.; Misra, S.; Qiu, T.; Lee, T.-C.; Mark, A. G.; *et al.* Applications of Three-Dimensional (3D) Printing for Microswimmers and Bio-Hybrid Robotics. *Lab Chip* **2015**, *15*, 1634–1637.

(45) Nawroth, J. C.; Lee, H.; Feinberg, A. W.; Ripplinger, C. M.; McCain, M. L.; Grosberg, A.; Dabiri, J. O.; Parker, K. K. A Tissue-Engineered Jellyfish with Biomimetic Propulsion. *Nat. Biotechnol.* **2012**, *30*, 792–797.

(46) Qiu, T.; Lee, T.-C.; Mark, A. G.; Morozov, K. I.; Münster, R.; Mierka, O.; Turek, S.; Leshansky, A. M.; Fischer, P. Swimming by Reciprocal Motion at Low Reynolds Number. *Nat. Commun.* **2014**, *5*, 5119.

(47) Qu, X.; Zhu, W.; Huang, S.; Li, Y. S.; Chien, S.; Zhang, K.; Chen, S. Relative Impact of Uniaxial Alignment vs. Form-Induced Stress on Differentiation of Human Adipose Derived Stem Cells. *Biomaterials* **2013**, *34*, 9812–9818.

(48) Li, J.; Huang, G.; Ye, M.; Li, M.; Liu, R.; Mei, Y. Dynamics of Catalytic Tubular Microjet Engines: Dependence on Geometry and Chemical Environment. *Nanoscale* **2011**, *3*, 5083.

(49) Dusenbery, D. B. *Living at Micro Scale : The Unexpected Physics of Being Small*; Harvard University Press, 2009.

(50) Burgess, A.; Vigneron, S.; Brioudes, E.; Labbé, J.-C.; Lorca, T.; Castro, A. Loss of Human Greatwall Results in G2 Arrest and Multiple Mitotic Defects due to Deregulation of the Cyclin B-Cdc2/PP2A Balance. *Proc. Natl. Acad. Sci.* **2010**, *107*, 12564–12569.

(51) Wang, H.; Zhao, G.; Pumera, M. Beyond Platinum: Bubble-Propelled Micromotors Based on Ag and MnO 2 Catalysts. *J. Am. Chem. Soc.* **2014**, *136*, 2719–2722.

(52) Solovev, A. A.; Sanchez, S.; Pumera, M.; Mei, Y. F.; Schmidt, O. C. Magnetic Control of Tubular Catalytic Microbots for the Transport, Assembly, and Delivery of Micro-Objects. *Adv. Funct. Mater.* **2010**, *20*, 2430–2435.

(53) Li, J.; Singh, V. V; Sattayasamitsathit, S.; Orozco, J.; Kaufmann, K.; Dong, R.;

Gao, W.; Jurado-sanchez, B.; Fedorak, Y.; Wang, J. Supporting Information of Water-Driven Micromotors for Rapid Photocatalytic Degradation of Biological and Chemical Warfare Agents. **2014**, 2–5.

(54) Gao, W.; Uygun, A.; Wang, J. Hydrogen-Bubble-Propelled Zinc-Based Microrockets in Strongly Acidic Media. *J. Am. Chem. Soc.* **2012**, *134*, 897–900.

(55) Tichý*, J.; Erhart, J.; Kittinger*, E.; Přívratská, J. Principles of Piezoelectricity. In *Fundamentals of Piezoelectric Sensorics*; Springer Berlin Heidelberg: Berlin, Heidelberg, 2010; pp. 1–14.

(56) Merry, R. J. E.; Maassen, M. G. J. M.; Van De Molengraft, M. J. G.; Van De Wouw, N.; Steinbuch, M. Modeling and Waveform Optimization of a Nano-Motion Piezo Stage. *IEEE/ASME Trans. Mechatronics* **2011**, *16*, 615–626.

(57) Ritter, T. A.; Shrout, T. R.; Tutwiler, R.; Shung, K. K. A 30-MHz Piezo-Composite Ultrasound Array for Medical Imaging Applications. *IEEE Trans. Ultrason. Ferroelectr. Freq. Control* **2002**, *49*, 217–230.

(58) Dargaville, T. R. T.; Celina, M. C.; Elliot, J.; Chaplya, P. M.; Elliott, J. M.; Jones, G. D.; Mowery, D. M.; Assink, R. a; Clough, R. L.; Martin, J. W. Characterization, Performance and Optimization of PVDF as a Piezoelectric Film for Advanced Space Mirror Concepts. *Optimization* **2005**.

(59) Jaffe, B.; Cook, W. R.; Jaffe, H. L. *Piezoelectric Ceramics*,; Academic Press: London ;New York, 1971.

(60) Savakus, H. P.; Klicker, K. A.; Newnham, R. E. PZT-Epoxy Piezoelectric Transducers: A Simplified Fabrication Procedure. *Mater. Res. Bull.* **1981**, *16*, 677–680.

(61) Brown, J. A.; Foster, F. S.; Needles, A.; Cherin, E.; Lockwood, G. R. Fabrication and Performance of a 40-MHz Linear Array Based on a 1-3 Composite with Geometric Elevation Focusing. *IEEE Trans. Ultrason. Ferroelectr. Freq. Control* **2007**, *54*, 1888–1894.

(62) Lee, K. Y.; Kim, D.; Lee, J. H.; Kim, T. Y.; Gupta, M. K.; Kim, S. W. Unidirectional High-Power Generation via Stress-Induced Dipole Alignment from ZnSnO3 Nanocubes/polymer Hybrid Piezoelectric Nanogenerator. *Adv. Funct. Mater.* **2014**, *24*, 37–43.

(63) Lee, S.; Bae, S. H.; Lin, L.; Yang, Y.; Park, C.; Kim, S. W.; Cha, S. N.; Kim, H.; Park, Y. J.; Wang, Z. L. Super-Flexible Nanogenerator for Energy Harvesting from Gentle Wind and as an Active Deformation Sensor. *Adv. Funct. Mater.* **2013**, *23*, 2445–2449.

(64) Kim, K.; Zhu, W.; Qu, X.; Aaronson, C.; McCall, W. R.; Chen, S. C.; Sirbuly, D. J. 3D Optical Printing of Piezoelectric Nanoparticle - Polymer Composite Materials. *ACS Nano* **2014**, *8*, 9799–9806.

(65) Takahashi, H.; Numamoto, Y.; Tani, J.; Matsuta, K.; Qiu, J.; Tsurekawa, S. Lead-Free Barium Titanate Ceramics with Large Piezoelectric Constant

Fabricated by Microwave Sintering. *Japanese J. Appl. Physics, Part 2 Lett.* **2006**, *45*.

(66) Simon-Seveyrat, L.; Hajjaji, A.; Emziane, Y.; Guiffard, B.; Guyomar, D. Re-Investigation of Synthesis of BaTiO3 by Conventional Solid-State Reaction and Oxalate Coprecipitation Route for Piezoelectric Applications. *Ceram. Int.* **2007**, *33*, 35–40.

(67) Serini, V. *Polycarbonates*; 2000; Vol. 29.

(68) Feng, J.; Zhuo, R. X.; Zhang, X. Z. Construction of Functional Aliphatic Polycarbonates for Biomedical Applications. *Prog. Polym. Sci.* **2012**, *37*, 211–236.

(69) Krishnan, A. V; Stathis, P.; Permuth, S. F.; Tokes, L.; Feldman, D. Bisphenol-A: An Estrogenic Substance Is Released from Polycarbonate Flasks during Autoclaving. *Endocrinology* **1993**, *132*, 2279–2286.

(70) Diamanti-Kandarakis, E.; Bourguignon, J.-P.; Giudice, L. C.; Hauser, R.; Prins, G. S.; Soto, A. M.; Zoeller, R. T.; Gore, A. C. Endocrine-Disrupting Chemicals: An Endocrine Society Scientific Statement. *Endocr. Rev.* **2009**, *30*, 293–342.

(71) Pyo, S. H.; Nuszkiewicz, K.; Persson, P.; Lundmark, S.; Hatti-Kaul, R. Lipase-Mediated Synthesis of Six-Membered Cyclic Carbonates from Trimethylolpropane and Dialkyl Carbonates: Influence of Medium Engineering on Reaction Selectivity. *J. Mol. Catal. B Enzym.* **2011**, *73*, 67–73.

(72) Pyo, S. H.; Hatti-Kaul, R. Selective, Green Synthesis of Six-Membered Cyclic Carbonates by Lipase-Catalyzed Chemospecific Transesterification of Diols with Dimethyl Carbonate. *Adv. Synth. Catal.* **2012**, *354*, 797–802.

(73) Pyo, S. H.; Hatti-Kaul, R. Chlorine-Free Synthesis of Organic Alkyl Carbonates and Five- and Six-Membered Cyclic Carbonates. *Adv. Synth. Catal.* **2016**, *358*, 834–839.

(74) Adireddy, S.; Lin, C.; Cao, B.; Zhou, W.; Caruntu, G. Solution-Based Growth of Monodisperse Cube-like BaTiO3 Colloidal Nanocrystals. *Chem. Mater.* **2010**, *22*, 1946–1948.

(75) Hajati, A.; Latev, D.; Gardner, D.; Hajati, A.; Imai, D.; Torrey, M.; Schoeppler, M. Three-Dimensional Micro Electromechanical System Piezoelectric Ultrasound Transducer. *Appl. Phys. Lett.* **2012**, *101*.

(76) Rajabi, A. H.; Jaffe, M.; Arinzeh, T. L. Piezoelectric Materials for Tissue Regeneration: A Review. *Acta Biomater.* **2015**, *24*, 12–23.